Cerebellar climbing fibers impact experience-dependent plasticity in the mouse primary somatosensory cortex

Authors: Abby Silbaugh[1], Kevin P. Koster[1], Christian Hansel[1]*

Affiliations:

[1]Department of Neurobiology and Neuroscience Institute, University of Chicago; Chicago, 60637, USA.

*Corresponding author. Email: chansel@bsd.uchicago.edu.

Summary

In the cerebellum, climbing fibers (CFs) provide instructive signals for supervised learning at parallel fiber to Purkinje cell synapses. It has not been tested so far whether CF signaling may also influence plasticity in other brain areas. Here, we show that optogenetic CF activation suppresses potentiation of whisker responses in L2/3 pyramidal cells in primary somatosensory cortex (S1) of awake mice that is observed after repeated whisker stimulation. Using two-photon imaging and chemogenetics, we find that CFs control plasticity by modulating SST- and VIP-positive interneurons in S1 cortex. Transsynaptic labeling identifies zona incerta (ZI) to thalamic posterior medial nucleus projections as a pathway for cerebellar output reaching S1 cortex. Chemogenetic inhibition of PV-positive neurons in the ZI prevents CF co-activation effects, identifying the ZI as a critical relay. Our findings demonstrate that CFs impact sensory signal processing and plasticity in S1 cortex and thus may convey instructive signals.

Keywords:

Calcium, Instructive signal, Parvalbumin-positive interneuron, Posterior medial thalamic nucleus, Purkinje cell, Pyramidal cell, Somatostatin-position interneuron, Supervised learning, Vasoactive intestinal polypeptide-positive interneuron, Zona incerta

Introduction

Sensory experience and learning are associated with plasticity of multiple brain regions. Neocortical plasticity canonically depends on the activity of its direct input structures[1]. For example, plasticity in the barrel field of the primary somatosensory cortex (S1 cortex) of rodents is evoked upon repeated whisker stimulation. Receptive field maps may reorganize after whisker clipping[2-4] or a history of rhythmic whisker stimulation[5-7] that necessitates adaptive plasticity of synaptic weights, e.g. via long-term potentiation (LTP) and/or long-term depression (LTD) at synaptic inputs onto pyramidal neurons[8, 9]. The high degree of plasticity in S1 somatosensory circuits enables adaptation to altered inputs[10]. Though experience-dependent plasticity in neocortex is highly responsive to input features, modulating influences from other brain regions may play a role.

The cerebellum is increasingly assigned functions that were previously attributed to the neocortex[11, 12]. It projects via the thalamus to motor cortex and non-motor areas, including the prefrontal cortex[13, 14], sensory, and associative areas[15-17]. A plausible possibility is therefore that cerebellar output impacts cortical signaling. It has indeed been shown that modulation of cerebellar outputs influences activity in the frontal cortex[18], coherence of neuronal oscillations between neocortical areas[19-21], and plasticity in parietal-motor cortex connections[22]. However, the cellular mechanisms of these interactions have not been described.

Here, we ask the specific question of whether cerebellar climbing fiber (CF) signals have the mechanistic capacity to impact neocortical plasticity. Our motivation to study CF signaling is rooted in the importance of their activity for normal cerebellar function, where CF-controlled plasticity represents a classic example of supervised learning in the brain[1]. Depending on dendritic architecture, Purkinje cells (PCs) receive input from one or more climbing fibers (CFs)[23] that originate in the contralateral inferior olive (IO). As originally predicted by Marr in his *Theory of Cerebellar Cortex*, CF signaling supervises plasticity at parallel fiber (PF) – PC synapses, providing *contexts* for learning[24]. It was later experimentally demonstrated that PF and CF co-stimulation initiates LTD at PF synapses[25-28], and that the CF – via evoked calcium transients – tightly controls plasticity at these synapses[29-34] and provides instructive signals for cerebellum-controlled learning[35-38]. CFs provide instructive error signals[39], convey sensory input across modalities[40-44], and may even signal the absence of expected sensory signals[45]. CFs may also carry reward or reward prediction-related signals[46, 47]. Contexts in which CFs are recruited continue to be identified, underscoring the importance of establishing whether they may influence neocortical activity and plasticity.

To determine whether CF signaling has the capacity to impact plasticity of S1 neurons, we use the mouse brain to give us experimental access at the cellular level. Our observation that CF signaling regulates plasticity of L2/3 pyramidal cells in S1 cortex shows that activity in the olivo-cerebellar system has distinct consequences for input processing and plasticity in S1 cortex, and significantly expands what is known about the basic interaction between these regions. This mechanism could be used to provide signals to neocortex that are instructive in nature, depending on the context in which CFs are recruited, similar to those signals that play a role in cerebellar supervised learning.

Activity-dependent plasticity in S1 cortex is regulated by optogenetic CF activation

To study the effects of CF activity on S1 plasticity, we expressed GCaMP6f in neurons in S1 cortex and used two-photon microscopy in awake mice to measure responses to air puff stimulation of the whisker field in layer 2/3 (L2/3) neurons (Figure 1A, D). For optogenetic CF activation, channelrhodopsin-2 (ChR2) was expressed in neurons of the inferior olive (IO), which give rise to CFs terminating in the contralateral cerebellar cortex (Figure 1B, E; Figure S1A, B). An LED was used to deliver 470nm light pulses over an optical window centered on crus I/II, an area of the cerebellar cortex responsive to stimulation of the ipsilateral whisker field[40]. The efficacy of optogenetic activation was tested by expressing GCaMP6f in PCs of crus I/II and measuring calcium transients evoked by LED light pulses, which we varied in frequency and duration to achieve optogenetically evoked signals resembling spontaneous CF transients (Figure 1C; Figure S1F). Single light pulses lasting 50ms evoked CF transients which were not significantly different in amplitude or peak latency from spontaneous events recorded in the same PCs (Figure S1H, I)[48]. For plasticity induction in S1 cortex, we used a multi-whisker stimulation protocol ('rhythmic whisker stimulation'; RWS) similar to those previously used to study sensory-driven synaptic plasticity *in vivo*[7, 9, 49, 50]. Here, RWS consisted of an application of 100ms air puffs (8psi) to the contralateral whisker field for 5min at 8Hz, a natural whisking frequency for mice that are sampling the environment[51]. RWS stimulation resulted in an increase in whisker-evoked calcium responses ($\Delta F/F$ over the range of 0-700ms post-stimulus onset) that we observed in morphologically identified L2/3 pyramidal neurons (PNs; Figure 1F) for the duration of the recording (60min post-RWS; Figure 1G-I). The somatic calcium response amplitudes measured with GCaMP6 correlate with neuronal spike rates[52]. L2/3 pyramidal neurons respond to stimulation of the corresponding principal whisker but may also respond to stimulation of surround whiskers[53]. Therefore, the plasticity observed here in response to multi-whisker stimulation may reflect both a potentiation of synapses conveying already existing whisker input as well as an expansion of the neuron's receptive field to include additional surround whiskers. Given increases in the activity of excitatory neurons may be coupled with decreased activity of local inhibitory neurons in this form of plasticity[54], we also assessed the responses of neurons that were not identified as pyramidal cells (i.e. putative interneurons; INs) in the same mice. Indeed, INs collectively responded to RWS stimulation with a significant depression in the amplitude of evoked calcium events (Figure 1J-L; Figure S2F, G). As parvalbumin (PV)-positive interneurons, somatostatin (SST)-positive interneurons, and vasoactive intestinal polypeptide (VIP)-positive interneurons make up ~40%, ~30%, and ~12% of the neocortical interneuron population[55, 56], respectively, this plasticity effect is likely comprised of a substantial portion of SST and PV interneurons. Using transgenic mice to tag SST and PV interneurons with tdTomato, we demonstrate RWS causes a significant depression in SST and PV interneurons (Figure S2H, I) – consistent with our observations in putative interneurons.

To determine whether CF co-activation with whisker stimulation influences this form of experience-dependent plasticity, 50ms light pulses were delivered at 1Hz during the 5min period of repeated whisker stimulation (RWS+CF), which is the rate of spontaneous CF discharge[39]. Each light pulse was delivered with a delay of 45ms with respect to the onset of whisker stimuli, mimicking the natural latency of CF responses to whisker stimulation[40]. RWS+CF blocked the potentiation of L2/3 pyramidal cell responses in S1 cortex and depression was observed instead (Figure 1G-I; Figure S2D, E). The depression of IN responses observed after RWS was absent upon optogenetic CF co-activation (Figure 1J-L, Figure S2F, G), and recordings in mice with tdTomato-tagged SST and PV interneurons further demonstrated the absence of inhibitory

interneuron depression (Figure S2H, I). Importantly, both the S1 plasticity and optogenetic CF activation effects were observed when trials with active movement of the mouse were included (Figure 1; Figures S2+3) or when analysis was restricted to trials during which the mice were resting both before stimulus onset and throughout the entire response period (Figure S3). Note movements of the vibrissae were absent during rest.

To test to robustness of these effects, we reproduced these findings using an alternate methodology that is well suited to detect receptive fields, including barrels in S1 cortex. Intrinsic optical imaging[57] was used to measure plasticity effects at low spatial resolution in anesthetized mice to facilitate measurement of single whisker responses. We slipped a glass pipette over an individual untrimmed whisker and moved it back and forth at 10Hz for a period of 5min. In the barrel field of contralateral S1 cortex, we confirmed the activation of the corresponding barrel and recorded responses to this passive sensory experience for 20min before and 30min after repeated stimulation. We observed an increase in the responsive area beyond the barrel that was not seen in the absence of repeated stimulation (Figure S4). When ChR2-expressing CFs in crus I/II of the cerebellum were optogenetically activated at 1Hz for 5min during the period of repeated stimulation, this plasticity was not observed in S1 cortex (Figure S4). Thus, intrinsic optical imaging demonstrates receptive field plasticity of barrels can be regulated by cerebellar signaling.

Taken together, our findings demonstrate that whisker-induced response potentiation in S1 cortex results from L2/3 pyramidal cell plasticity. Local inhibitory interneurons show the opposite direction of plasticity in the same animals. The observation that this IN plasticity is of lower amplitude and does not perfectly mirror pyramidal cell plasticity suggests that the former supports the latter and may help to control it, but that pyramidal cell LTP may take place even in the absence of LTD in IN neurons. CF activity regulates this form of whisker map plasticity. Note that 'LTP' and 'LTD' here reflect target neuron responsiveness – as measured by neural calcium signals – and are not specifically shown to rest on synaptic gain changes.

CF activation modulates inhibitory interneurons in S1 cortex

Local inhibitory interneurons regulate the activity and plasticity of neocortical pyramidal neurons, phenomena studied extensively in the rodent barrel cortex[56]. Thus, to identify the potential mediators of the gating effect of optogenetic CF activation on S1 plasticity, we next determined how the basic whisker response properties of specific neuron types in the S1 circuit are altered during CF co-activation (Figure 2A). To begin, we demonstrated that these basic responses are not significantly changed in the population of examined L2/3 pyramidal neurons upon optogenetic CF activation (Figure 2B; 0-700ms analysis window). However, we found that in 11/23 mice, an overall response decrease resulted from CF co-activation, while in 5/23 mice an increase was seen (using a 10% threshold). Significance in the observed mild response reduction emerged in the analysis across all neurons when a late analysis window was selected (650-850ms, selected as an early component of the post-peak response). These findings suggest that CF co-activation causes a range of response changes in the population of L2/3 pyramidal neurons, but that an overall suppressive effect becomes apparent in the late response phase.

In the same mice, the basic responses of INs to whisker stimulation were increased upon CF co-activation (Figure 2C). Like the plasticity effects measured in the IN populations (Figure 1J-L), these basic response increases are likely comprised of a majority of PV and SST interneurons.

157 Using tdTomato-tagged interneurons to identify SST and PV interneurons (Figure 2D-F), we
158 showed that basic responses to whisker stimulation were indeed enhanced in SST and PV
159 interneurons upon CF co-activation (Figure 2G-I). VIP interneurons – which primarily inhibit
160 other interneurons including SSTs and PVs[56] – showed no consistent change in their basic
161 responses to whisker stimulation upon CF co-activation in the default analysis window (0-
162 700ms; Figure 2G). However, like pyramidal neurons (Figure 2B), VIPs demonstrated
163 significant suppression in the late analysis window of 650-850ms (Figure 2G).

164 **Opposing roles of SST and VIP interneurons in CF-mediated control of S1 plasticity**

165 As SST interneurons are activated by CF co-activation, we tested whether they assume a key role
166 in the CF-mediated regulation of S1 plasticity. To do so, we next used chemogenetic approaches
167 for activity manipulation. We focused on SST interneurons because they contact the dendrites of
168 L2/3 pyramidal cells (Figure 3A, E), where inhibition can impact local synaptic plasticity
169 processes. We first expressed the excitatory hM3D(Gq) DREADD in neocortical SST
170 interneurons (Figure 3B). Administration of the DREADD agonist deschloroclozapine (DCZ) by
171 intraperitoneal injection caused an increase in SST interneuron responses (Figure 3C). Under
172 these conditions, RWS did not potentiate L2/3 pyramidal cell responses and calcium signals were
173 depressed instead (Figure 3D), mimicking the results of optogenetic CF co-activation (Figure
174 1G-I). In contrast, inhibitory hM4D(Gi) DREADD expression in SST interneurons (Figure 3F)
175 and acute administration of DCZ caused a significant reduction in SST interneuron responses
176 (Figure 3G). This rescued potentiation of L2/3 pyramidal cell responses when RWS was paired
177 with CF co-activation (Figure 3H). These findings confirm that SST interneurons are positioned
178 to control plasticity of L2/3 pyramidal neurons[9] and suggest that this mechanism is recruited by
179 CF co-activation.

180 SST interneurons receive relatively weak input from cortical and subcortical regions providing
181 input to S1 but are strongly inhibited by VIP interneurons (Figure 4A, E)[58, 59]. VIP interneurons
182 may suppress SST activity during RWS, thus enabling plasticity[9, 60]. We have shown above that
183 optogenetic CF activation reduces whisker-evoked responses in a subset of VIP interneurons
184 (Figure 2G). To examine whether this activity regulation is critical for RWS+CF-induced
185 suppression of L2/3 pyramidal cell plasticity, we used chemogenetic approaches to manipulate
186 the activity of VIP interneurons. We first observed that expression of inhibitory hM4D (Gi)
187 DREADDs in VIP interneurons (Figure 4B) and acute DCZ administration significantly reduced
188 activity in VIP interneurons (Figure 4C) and prevented S1 potentiation upon RWS stimulation
189 alone (Figure 4D). This manipulation was similar to the effect of RWS+CF (Figure 1G-I) or SST
190 activation during RWS (Figure 3D). Conversely, expression of excitatory hM3D(Gq) DREADDs
191 in VIP interneurons (Figure 4F) and acute DCZ administration enhanced VIP interneuron
192 responses (Figure 4G) and rescued S1 plasticity upon paired RWS and optogenetic CF activation
193 (RWS+CF; Figure 4H), mimicking the effect of RWS (Figure 1G-I) or suppression of SST
194 interneuron activity during RWS+CF (Figure 3H).

195 To control for the continued presence of DCZ, identical experiments for each condition were
196 performed without the administration of RWS (Figure S5A, D) or RWS+CF (Figure S5G, J, M).
197 When comparing control and plasticity experiments, both the SST activation and VIP
198 inactivation experiments successfully show SST activation is sufficient to block RWS-mediated
199 PN potentiation (Figure S5C), and VIP activity is required for RWS-mediated PN potentiation

(Figure S5F). The VIP activation experiments also successfully showed VIP activation rescues PN potentiation after RWS+CF (Figure S5O), and that this effect and was not due to sustained increases in responsivity of pyramidal neurons caused by the presence of DCZ in these conditions (Figure S5N). We additionally tested the potential contribution of PV interneurons to the CF-mediated control of S1 plasticity. Expression of inhibitory hM4D (Gi) DREADDs in PV interneurons indeed rescued PN potentiation after RWS+CF when compared to controls (Figure S5L), a robust effect given that PV interneurons are usually basket cells with strong recurrent connectivity to pyramidal neurons[56]. To support our interpretation that VIP interneurons control a disinhibitory network in S1 cortex, we further analyzed the IN populations (which consist of putative SSTs and PVs) in the VIP chemogenetic manipulation experiments (Figure 5). VIP inactivation during RWS, which blocked PN potentiation (Figure 4D), indeed caused a corresponding increase in IN activity (Figure 5C) to mimic the effects of RWS+CF (Fig. 1G-L) even without CF activity. VIP activation during RWS+CF, which rescued PN potentiation (Figure 4H), caused a corresponding decrease in IN activity (Figure 5F) to mimic the effects of RWS (Figure 1G-L) even when CFs were active. These findings confirm that VIP interneurons orchestrate the inhibitory network in S1 cortex and show that this mechanism is recruited by optogenetic CF activation. Taken together, the findings presented thus far show that the critical circuit for RWS-driven plasticity is located in S1 cortex itself and identify VIP and SST interneurons as effectors that are sufficient to mediate the consequences of CF activation. The notion of sufficiency does not exclude potential effects of plasticity processes elsewhere that might well modulate effector activation in this context and others not tested here.

Zona incerta to the thalamic posterior medial nucleus (POm) as a multi-synaptic pathway from the cerebellar nuclei to S1 cortex

Cerebellar climbing fibers must exert their effects on the neocortex via the deep cerebellar nuclei (DCN), beyond which there may be several potential pathways to the primary somatosensory cortex. The barrel cortex in mice receives whisker sensory information from two thalamic sources, the ventral posterior medial thalamic nucleus (VPM), and the posterior medial thalamic nucleus (POm). Whereas the VPM projects densely to the middle layers of S1 cortex, POm inputs terminate largely in L5 as well as L1, where, in addition to pyramidal cells, they synapse on VIP interneurons[58, 59]. POm-to-VIP inputs have previously been shown to gate RWS-mediated plasticity of PNs in barrel cortex[50]. However, because the DCN send only weak direct projections to POm (and VPM), we focused on other output regions of the cerebellum that could influence the activity of sensory thalamic nuclei: the thalamic reticular nucleus (TRN) and zona incerta (ZI). The ZI represents a more plausible pathway through which the CF could exert its effects on S1 given its robust innervation by the cerebellar nuclei[17, 61, 62] and projections to the POm[63]. To rule out a pathway to S1 through the thalamic reticular nucleus, whose GABAergic neurons primarily inhibit VPM[64], we used retrograde fluorogold labeling from the somatosensory thalamus (which included VPM and POm) and anterograde labeling from the contralateral DCN. We found no overlap in the TRN (Figure S6). Next, we determined the primary output pathways of ZI cells that receive cerebellar input by using a dual-injection approach which leveraged the transsynaptic transport properties of AAV1[65]: AAV1-Flp recombinase (pAAV-EF1a-Flpo) was delivered to the deep cerebellar nuclei, followed by a Flp-dependent label (Frt-ChR2-EYFP) to contralateral ZI. Abundant EYFP-expressing neurons were found in the ZI (Figure 6A, B; Figure S7), with their axon terminals visible in both POm (Figure 6A, B; Figure S7) and S1 cortex

(Figure 6A, B). These results suggest that the ZI-POm pathway, and not the TRN-VPM pathway, constitutes a critical thalamic route for cerebellar signals reaching S1 cortex (Figure S6C).

To assess whether there is a monosynaptic connection from the cerebellar nuclei to neurons in the ZI that project to POm, we induced ChR2 expression in the cerebellar nuclei and performed *in vitro* whole-cell patch-clamp recordings from POm-projecting ZI neurons (i.e. cells that were retrogradely labeled by fluoro-Ruby injected into POm) and tested them for ChR2-evoked responses (Figure 6D, Figure S8). Optogenetic activation of ChR2+ terminals at 10Hz elicited EPSPs that persisted in the presence of bath-applied TTX (1 μM; Figure 6E, F), despite significant amplitude reduction. This TTX-insensitive component represents the ChR2-evoked EPSP at the synapses between cerebellar nuclei neurons and ZI neurons and demonstrates the monosynaptic nature of this pathway[66].

It has previously been demonstrated that most POm-projecting neurons in ZI are PV neurons[67]. To test whether these neurons convey cerebellar instructive signals to S1 cortex, we chemogenetically inhibited PV neurons in ZI during basic whisker and whisker plus optogenetic CF activation conditions and measured responses in L2/3 pyramidal neurons in S1 cortex. Expression of inhibitory hM4D (Gi) DREADDs in ZI-residing PV neurons (Figure 6G) and DCZ application prevented the suppressive effect of CF co-activation on pyramidal cell responses (Figure 6H, I). These data demonstrate that thalamically projecting PV neurons in ZI convey CF signals to S1 cortex.

Discussion

Multiple functions have been assigned to cerebellar CFs. As in our recordings, optogenetic CF co-activation suppresses S1 pyramidal neuron plasticity in an experimental paradigm lacking behavioral reward, this behaviorally neutral signal acts like an error signal would. However, it remains possible that CF recruitment and regulation of S1 plasticity may happen in a reward / reward omission context as well. CF activation might be driven by reward / reward omission in sensory-association training. This might be the reason why sensory stimulation in such training context drives cortical plasticity less well than passive sensory stimulation alone[68]. Plasticity in S1 cortex results from an update in sensory input – here exposure to a new sensory experience, prolonged rhythmic whisker activation at 8Hz – that necessitates circuit adaptation. CF signaling may get recruited when an obvious disruption or violation of a sensory prediction occurs, or simply when no stability in sensory input is reached. The absence of *sameness* may be detected by inferior olive neurons as an error in the sensory environment, and subsequently CFs prevent the otherwise unfolding potentiation. Such function provides an example for a "sensory role" of the olivo-cerebellum[69,70], in this case by controlling adaptive plasticity in a primary sensory cortex, without immediate effects on the motor domain.

In rodents, direct trigemino-olivary connections convey whisker-related information to the olive[71]. Passive whisker activation evokes CF-mediated complex spike firing in PCs in ipsilateral crus I/II[40]. These evoked spikes occur on top of a spontaneous complex spike firing rate of ~1Hz[39]. What distinguishes CF activity that suppresses plasticity in the cerebral cortex from these more common activity patterns? First, prolonged low-frequency air puff stimulation to sensitive skin areas on the snout or wrist of rodents evokes potentiation, and not depression, of PC responses[72, 73]. This finding is in line with the current understanding of CF signaling: novelty activates it[39]; when stimuli are repeatedly presented (producing/inhabiting a state of *sameness*),

evoked complex spike firing weakens. Thus, RWS stimulation likely will not produce continuous elevated CF activation. For this to happen under natural conditions, novel input features have to emerge. Second, the synchronization of CF responses might be critical. Complex spike synchrony is absent or weak during spontaneous activity and might increase with movement initiation[74, 75] or sensory stimulation[76]. Synchrony in a sufficiently high number of PCs is needed to evoke inhibition and subsequent rebound excitation in target neurons in the cerebellar nuclei[77, 78]. Parallel fibers (PFs) likely cannot generate synchronous activity in enough PCs due to the spatial arrangement of PF input[79]. A threshold level of synchronization will be reached with optogenetic CF activation but may also naturally be reached with specific qualities of the sensory input signal, e.g. those that make it an error signal. It is also conceivable that synchronization to a threshold level is driven by an error signal that does not originate from whisker stimulation but has another sensory or non-sensory origin.

Whisker-related sensory information in rodents is conveyed by the trigeminal ganglion via thalamic nuclei VPM and POm to the barrel cortex; information from specific whiskers is projected via VPM to cortical layer 4[80]. The observation that cerebellar signals impact S1 cortex via ZI and POm fits the description of a more modulatory pathway that does not interfere with thalamic input in layer 4, but with synaptic signal integration in the more superficial as well as deeper layers. Both two-photon imaging and chemogenetics identify SST interneurons in S1 cortex as the ultimate effectors of the activation of this modulatory pathway (note that a similar mechanism might underlie a phenomenon clinically known as CBI or 'cerebellar-brain-inhibition', where electrical or magnetic stimulation over the cerebellum in human subjects causes a reduction in excitability of the motor cortex[81, 82]). SST interneurons, in turn, are regulated by VIP interneurons that receive activation from POm[59]. We identified PV neurons in ZI as neurons that are critically involved in this pathway as well, likely reducing the POm-mediated activation of VIP interneurons in S1 cortex. Our findings demonstrate that cerebellar output may recruit PV neurons in ZI sufficiently well to ultimately cause a removal of VIP interneuron-mediated inhibition of SST interneurons and consequently enhance dendritic inhibition of L2/3 pyramidal neurons. This activation sequence likely requires an initial activation of excitatory neurons in the cerebellar nuclei by output from the cerebellar cortex, which may result from rebound excitation following synchronous PC activity[78]. Another context where PV neurons in the ZI become activated – via glutamatergic input from S1 cortex – is self-grooming in the orofacial area[83]. It is plausible that under such conditions of predicted sensory input, whisker-related L2/3 pyramidal neuron plasticity is suppressed as well. While our findings identify the cerebellar nuclei to ZI to POm projection as critical to conveying CF signals to S1 cortex, it is likely that more projections that are not tested here can provide links from the cerebellum to S1 cortex. This is suggested by the distinct multi-channel output from the cerebellar nuclei[84]. For example, we cannot exclude a participation of direct projections from the cerebellar nuclei to VPM or POm[85] (note, however, the prominence of projections that reach the ZI and originate in the cerebellar nuclei, as shown in Figure 6A-C; Figure S7). Moreover, it remains possible that cerebellar output reaches S1 cortex via M1 cortex, as both cortices show strong reciprocal connections[86] and S1-projecting pyramidal neurons in M1 target VIP interneurons in S1 cortex[87].

Our data show that activity of cerebellar CFs has an impact on S1 cortex, preventing plasticity of L2/3 pyramidal neurons via the recruitment of local SST interneurons. In our experiments, CFs were artificially (optogenetically) stimulated, and definitive conclusions about CF engagement and its consequences under natural conditions remain open. However, our study demonstrates

333 both the capacity for such impact on cortical signaling and a pathway that enables this impact.
334 These are requirements for CF signals to act as instructive signals in supervised learning[88]. A
335 condition for such an effect likely is a synchronization of CF responses in groups of PCs[77, 78], a
336 scenario that provides a qualifying distinction from other CF activity patterns[74-76]. The observed
337 external influence enables regulatory control that might safeguard the cerebral cortex from
338 maladaptation, albeit at the cost of exposing it to pathological dysfunction of the olivo-cerebellar
339 system, e.g. sensory over-responsivity that has been described in syndromic autism[48].

340 **Materials and Methods:**

341 **Animals**

342 All animal experiments were approved and conducted in accordance with the regulations and
343 guidelines of the Institutional Animal Care and Use Committee of the University of Chicago
344 (IACUC 72496). Mice were housed on a 12-hour light/dark cycle and fed a standard rodent diet.
345 Animals of either sex were used in all experiments and no sex-dependent differences were
346 observed in any reported measures. Strains included wildtype mice (C57BL/6J; Jax: 000664),
347 PVCre mice (B6.129P2-Pvalbtm1(cre)Arbr/J; Jax: 017320), SSTCre mice (STOCK
348 Ssttm2.1(cre)Zjh/J; Jax: 013044), VIPCre mice (B6J.Cg-Viptm1(cre)Zjh/AreckJ; Jax: 031628),
349 and Ai9 mice (B6.Cg-Gt(ROSA)26Sortm9(CAG-tdTomato)Hze/J; Jax: 007909). Homozygous
350 SSTCre, PVCre, and VIPCre animals were bred with wild type animals to generate
351 heterozygotes. To generate SST and VIP reporter lines ($SSTCre^{tdTom}$ and $VIPCre^{tdTom}$),
352 homozygous SSTCre and VIPCre mice were bred with homozygous Ai9 mice. Only
353 heterozygous animals were used for experiments given evidence that endogenous somatostatin
354 (SST) and vasoactive intestinal polypeptide (VIP) expression may be reduced in homozygous
355 SSTCre and VIPCre animals, respectively[89, 90].

356 **Stereotaxic injections**

357 **For electrophysiological experiments.** Stereotaxic virus injections for electrophysiological
358 experiments were performed as previously described using C57BL/6J mice between postnatal
359 day 23-28[91]. For optogenetics experiments in which cerebellar inputs to zona incerta were
360 measured, a 250 nL (40 nL/min) infusion of AAV5-hSyn-hChR2(H134R)-EYFP (UNC Vector
361 Core) was made into the right deep cerebellar nuclei (-1.5 ML; -5.8 AP; -3.2 DV[92]) using a 1 mL
362 Hamilton syringe (catalog: 65458-02) with a flat needle tip. Next, a small infusion (40 nL total,
363 at 7nL/min) of fluoro-Ruby (ThermoFisher, catalog: D1817) was made into left posterior medial
364 thalamus using a 0.5 mL Hamilton syringe (catalog: 65457-01). Following a two-week
365 incubation, animals were sacrificed for recordings in acute slices (see *Slice electrophysiology*).

366 **For tracing experiments.** For anterograde transsynaptic labeling experiments, a dual-injection
367 approach was utilized to specifically label the outputs of neurons in the zona incerta that receive
368 input from the contralateral cerebellar nuclei. Flpo-recombinase (AAV1-EF1a-Flpo, item#:
369 55637, Addgene) was injected into left deep cerebellar nuclei as above (+1.5 ML; -5.8 AP; -3.2
370 DV), followed by an infusion of AAV1-Flp-on ChR2-EYFP (AAV-hSyn-Coff/Fon-
371 hChR2(H134R)-EYFP-WPRE, UNC Vector core) into right zona incerta (-1.8 ML; -2.0 AP; -4.0
372 DV). Following a 5-week incubation – the period required for anterograde transport of the

AAV1 virus injected into zona incerta – animals were transcardially perfused for histology (see *Tissue preparation for fluorescence microscopy and immunohistochemistry*).

To visualize potential overlap between cerebellar terminals and cells in thalamic nuclei (i.e. the thalamic reticular nucleus) that project to somatosensory thalamus (ventral posteromedial nucleus and posterior medial thalamus), an orthograde virus (AAV5-hSyn-hChR2(H134R)-EYFP (UNC Vector core)) was injected into the right deep cerebellar nuclei (-1.5 ML; -5.8 AP; -3.2 DV) and fluorogold (2% w/v in sterile saline, Fluorochrome) was injected into the left somatosensory thalamus (primarily posterior medial thalamus). Following a 2-week incubation, animals were transcardially perfused for histology (see *Tissue preparation for fluorescence microscopy and immunohistochemistry*).

For two-photon calcium imaging experiments. Viral injections were performed to express channelrhodopsin-2 in cerebellar climbing fibers; fluorescent calcium indicators in cerebellar Purkinje cells or primary somatosensory (S1; barrel) cortex neurons; tdTomato, activating DREADDs, or inactivating DREADDs in S1 cortex; and inactivating DREADDs in interneurons in zona incerta. With respect to the inferior olive injection site (conferring viral expression in climbing fibers terminating in the contralateral cerebellar hemisphere), injections into cerebellar cortex were performed contralaterally, and injections into zona incerta and somatosensory cortex were performed ipsilaterally.

To express channelrhodopsin-2 in cerebellar climbing fibers, ChR2-EYFP (AAV9-CaMKIIa-hChR2(H134R)-EYFP; Addgene #26969-AAV9) or ChR2-mCherry (pAAV9-CaMKIIa-hChR2(H134R)-mCherry; Addgene #26975-AAV9) was injected into the left inferior olive as follows: after surgical preparation (see *Two-photon calcium imaging: Cranial window surgeries*), tissues attached to the occipital bone were surgically detached, followed by opening of the posterior atlanto-occipital membrane to expose the dorsal medulla. A 5µL Hamilton Neuros syringe (catalog: 65460-03) with a 33-gauge beveled needle tip (catalog: 65461-02) was inserted into the left medulla at an angle of 58-59° to the perpendicular line (Supplementary Data 2a), 0.75 mm laterally and 1.70 mm deep from the surface of the medulla as previously described[93]. A total volume of 400 nL was infused at a rate of 80 nL/min, and the syringe was held in place for five minutes before removal. ChR2-EYFP or ChR2-mCherry was chosen based on the excitation and emission spectra of other fluorophores expressed in the same animal to maximize signal separation when conducting post-hoc confocal imaging.

Stereotaxic virus injections for imaging of Purkinje cell dendrites were administered as previously described using P80-120 adult C57BL/6J mice[73]. A virus mixture was prepared with 0.5% L7-Cre (AAV1.sL7.Cre.HA.WPRE.hGH.pA, Princeton Neuroscience Institute Viral Core Facility, kindly provided by the lab of Dr. Samuel Wang at Princeton University), and 20% Cre-dependent GCaMP6f (AAV1.CAG.Flex.GCaMP6f.WPRE.SV40; Addgene, #100835) in saline solution. A glass pipette with a tip diameter of ~300 µm was prepared by a puller (model P-97, Sutter Instrument Co.) and used to inject a total volume of 1800 nL into two separate injection sites: 900 nL were injected into right medial Crus I (-1.8 ML; -7 AP; -1.8 DV), followed by a 900 nL injection into right medial Crus II (-2.5 ML; -7 AP; -2.2 DV). The pipette carrying the AAV virus was held in place for five minutes before withdrawal.

For DREADD suppression of PV interneurons in zona incerta, a 1 mL Hamilton syringe was used to infuse Cre-dependent hm4D(Gi) (AAV5-hSyn-DIO-hM4D(Gi)-mCherry; Addgene #44362-AAV5) into the left zona incerta (1.8 ML; -2.0 AP; -4.0 DV) of PVCre animals.

417 To express GCaMP6f in primary somatosensory (barrel) cortex neurons in C57BL/6J,
418 SSTCre^{tdTom}, and VIPCre^{tdTom} animals, a 5µL Hamilton Neuros syringe with a 33-gauge beveled
419 needle tip was used to infuse a total volume of 800 nL of GCaMP6f
420 (AAV1.Syn.GCaMP6f.WPRE.SV40; Addgene #100837-AAV) at two separate injection sites:
421 400 nL were injected at -1.2 AP; 2.5 ML and 400 nL at -1.5 AP; 3 ML. At each injection site,
422 200 nL were first injected 300 µm below the pial surface, followed by 200 nL at 150 µm below
423 the pial surface. The injections were performed at a rate of 100nL/minute, and the syringe was
424 held in place for five minutes before removal. To express GCaMP6f in barrel cortex neurons
425 with co-expression of tdTomato in parvalbumin (PV)-, SST-, and VIP-expressing interneurons in
426 PVCre, SSTCre, or VIPCre animals, respectively, GCaMP6f (Addgene #100837-AAV1) and
427 Cre-dependent tdTomato (AAV9-FLEX-tdTomato; Addgene #28306-AAV9) were co-injected
428 using the same technique. To optimize co-expression of the viruses, GCaMP6f with tdTomato
429 was mixed at a 3:1 volume ratio. For DREADD activation or suppression of VIP, SST, or PV
430 interneurons, Cre-dependent hM3D(Gq) (AAV5-hSyn-DIO-hM3D(Gq)-mCherry; Addgene
431 #44361-AAV5) or Cre-dependent hM4D(Gi) (AAV5-hSyn-DIO-hM4D(Gi)-mCherry; Addgene
432 #44362-AAV5) were used in place of tdTomato, respectively.

433 For all two-photon imaging experiments, recordings began after a 4-week incubation period after
434 the final virus injection (see *Two-photon calcium imaging: cranial window surgeries for detail*).

435 **Tissue preparation for fluorescence microscopy and immunohistochemistry**

436 After completion of two-photon experiments, selected animals (all those used in DREADD and
437 cerebellar imaging experiments, and a subset of animals in all other experimental cohorts) were
438 sacrificed for post-hoc characterization of viral expression. Animals were transcardially perfused
439 with ice-cold 4% paraformaldehyde in phosphate-buffered saline (25mL), pH 7.4. The brain was
440 extracted and postfixed in 4% paraformaldehyde overnight at 4°C before being transferred to a
441 cold 30% sucrose (in phosphate-buffered saline) solution for >48 hours. Brains were then
442 cryosectioned at 50 µm thickness, with an approximately equal number of brains sectioned
443 coronally or sagittally per experimental cohort. For tracing experiments, animals were perfused
444 with ice-cold phosphate-buffered saline (25mL) prior to perfusion with paraformaldehyde and
445 cryosectioned coronally at 150 µm thickness. Slices were stored in phosphate-buffered saline
446 prior to immunohistochemistry or confocal imaging.

447 For post-hoc visualization of Purkinje cells in mice expressing ChR2-EYFP in climbing fibers
448 (i.e. in animals without GCaMP6f expression in Purkinje cells), calbindin immunohistochemical
449 staining was performed. Tissue slices were washed in a 0.01M phosphate-buffered saline
450 solution containing 200 mM glycine for two hours at 4°C, then incubated in a 0.01M phosphate-
451 buffered saline solution containing 10 mM sodium citrate and 0.1% Tween-20 at ~60°C for 30
452 minutes using a heated water bath. After cooling to room temperature, the slices were washed
453 three times in a 0.01M phosphate-buffered saline solution containing 0.5% Tween-20 (PBS-
454 Tween) at room temperature for a period of 15 minutes per wash. Tissue was permeabilized with
455 200 mM glycine in PBS-Tween for 15 minutes at room temperature. Blocking was done for two
456 hours at room temperature with a PBS-Tween solution containing 5% bovine serum albumin and
457 10% normal donkey serum, followed by overnight incubation (12-15 hours) at 4°C in a PBS-
458 Tween solution containing 1% normal donkey serum and guinea pig anti-calbindin primary
459 antibody (1:500; Synaptic Systems Cat# 214 004, RRID:AB_10550535). After washing the

460 tissue three times for fifteen minutes in PBS-Tween at 4°C, slices were incubated for two hours
461 at 4°C in PBS-Tween containing 1% normal donkey serum and donkey anti-guinea pig Cy3
462 (555) secondary antibody (1:200; Jackson ImmunoResearch Labs Cat# 706-165-148,
463 RRID:AB_2340460). Finally, the slices were washed three times in PBS-Tween (ten minutes per
464 wash) before mounting with Vectashield (Vector Laboratories, Inc.). The mounted slices were
465 allowed to set overnight before imaging.

466 To confirm the channelrhodopsin-2 expression observed in cerebellar cortex was indeed
467 expressed in climbing fiber terminals, a subset of tissue was additionally labeled with VGluT2.
468 VGluT2 (rabbit anti-VGluT2, 1:500; Thermo Fisher Scientific Cat# 42-7800,
469 RRID:AB_2533537*)* was added to the primary antibody solution and donkey anti-rabbit AF647
470 (Jackson ImmunoResearch Labs Cat# 711-605-152, RRID:AB_2492288) was added to the
471 secondary antibody solution.

472 **Confocal imaging**

473 **Image acquisition.** Z-stack confocal images were taken at 5x (Olympus MPlan N 0.1NA, air),
474 10x (Zeiss Achroplan 0.25NA, air), 20x (Olympus UMPlanFL N 0.5NA, water), 40x (Zeiss EC
475 Plan-Neofluar 1.3NA, oil immersion), and 63x (Zeiss W Plan-Apochromat, water)
476 magnifications with a Zeiss LSM 900 Axio Examiner.Z1 scope. A subset of images (Figure 1e
477 and Figure S1B) were taken with a Zeiss LSM 5 Exciter, Axioskop 2 (using the 20x Olympus
478 UMPlanFL and 40x Zeiss EC Plan-Neofluar objectives, respectively). The images in Figure 6d
479 (shown with channel separation in Figure S8b) and Figure S6 were taken with a second Zeiss
480 LSM 900 confocal microscope. To facilitate direct comparison, images shown in series (as in
481 Figure 6c and Figure S7f) were taken with identical hardware and software configurations,
482 available in the image metadata.

483 **Post-hoc image processing.** To stitch multiple images (as in Figures 1B, 1D, 2D-F (right), 4B,
484 4F, 6B, 6C, S1A (top), S1E, S6A, S6B (top and bottom left), and S7C-E), a series of pairwise
485 stiches were performed using Fiji (NIH). Figure 1B and Figure S1A (top) each consisted of 4
486 images (each 5x magnification, 1024 x 1024 pixels). Figure 1D consisted of 12 images (each 5x
487 magnification, 512 x 512 pixels). Figure 2D (right) consisted of 10 images (each 10x
488 magnification, 1024 x 1024 pixels). Figures 2E and 2F (right) each consisted of 8 images (each
489 10x magnification, 512 x 512 pixels). Figures 4B and 4F each consisted of 2 images (each 20x
490 magnification, 512 x 512 pixels). Figure 6B (also shown as the first image in Figure S7D), and
491 all images in S7D and S7E each consisted of 6 images (each 5x magnification, 512 x 512 pixels).
492 Images in Figure 6C each consisted of 9 images (each 10x magnification, 512 x 512 pixels).
493 Figure S1E consisted of 8 images (each 5x magnification, 1024 x 1024 pixels). S7C consisted of
494 10 images (each 40x magnification, 512 x 512 pixels). Note a subset of the final stitched images
495 displayed in figures are cropped to show relevant detail.

496 Channel colors set during image acquisition followed conventional emission wavelength
497 assignments (i.e. red to indicate tdTomato, green to indicate GCaMP6f, etc.). To illustrate
498 interneuron subtypes and continuity across experiments (e.g., cyan to indicate ChR2 expression
499 across all optogenetic stimulation experiments), channel colors were specified post-imaging
500 using Fiji by separating channels and selecting the appropriate color when merging, ignoring
501 source LUTs. When necessary, post-hoc brightness and contrast adjustments were applied
502 linearly to an entire image – *after* stitching, if applicable – using Fiji. To facilitate direct

503 comparison, identical linear brightness/contrast adjustments were made across all images shown
504 in series (as in Figure 6C, Figure S7D, and Figure S7E).

505 To measure terminal density across the sections shown in Figure 6c, Fiji was used to rotate each
506 image such that the axis separating ventral from dorsal zona incerta was horizontal. A 400 µm x
507 1 mm region of interest (ROI) was drawn around the zona incerta, and each row of pixels within
508 this ROI was separated to facilitate calculation of the integrated density across each row of
509 pixels. A similar method was used to quantify the terminal density of cerebellar inputs to zona
510 incerta as in Figure S8. Briefly, images of sections matched for their rostro-caudal location were
511 rotated as before. Then, five line-ROIs oriented vertically, each being 200 µm wide, were
512 positioned side-by-side across the mediolateral axis of the zona incerta, and the spatial pattern of
513 fluorescence along these lines was measured by calculating the mean grey value along their
514 length (which was roughly 400 µm from the dorsal boundary to the ventral boundary). These
515 were averaged for each animal used. Shading represents SEM for both measurements.

516 **Slice electrophysiology**

517 **Acute slice preparation and whole cell recordings.** For recordings in acute slice, injected
518 animals (see *Stereotaxic injections: For electrophysiological experiments*) were deeply
519 anesthetized using the isoflurane drop method in a bell jar (with a raised platform for the animal)
520 and immediately transcardially perfused with 8-10 mL of ice cold oxygenated (95% O_2, 5%CO_2)
521 artificial cerebrospinal fluid, which contained the following (in mM): 125 NaCl, 25 $NaHCO_3$, 3
522 KCl, 1.25 NaH_2PO_4, 1 $MgCl_2$, 2 $CaCl_2$, and 25 glucose. The brain was then extracted, glue-
523 mounted on a vibratome (Leica) platform and blocked for coronal slices using an agarose (5%)
524 cube and sliced in the same solution (ice-cold). Slices were cut to 365 µm thickness. The brain
525 slices were then transferred to 32-34 °C oxygenated artificial cerebrospinal fluid that was
526 allowed to return to room temperature over the course of one hour, which constituted the slice
527 recovery period.

528 Slices containing the zona incerta and terminals from the cerebellar nuclei inputs were visualized
529 using differential interference contrast with an Axioskop 2FS microscope (Carl Zeiss).
530 Fluorescence from ChR2-EYFP expression and from retrograde fluoro-Ruby labeling was
531 confirmed using the 5x air objective and guided recording locations in zona incerta. Recordings
532 were made with a Multiclamp 700B amplifier and pCLAMP software (Molecular Devices).
533 Recording glass pipettes with 7–9 MΩ resistance were filled with an internal solution as follows
534 (in mM): 117 K-gluconate, 13 KCl, 1 $MgCl_2$, 0.07 $CaCl_2$, 10 Hepes, 0.1 EGTA, 2 Na_2-ATP, 0.4
535 Na-GTP, pH 7.3, 290 mOsm. Incertal cells whose morphology was clearly revealed by strong
536 red fluorescence, indicating retrograde labeling from posterior medial thalamus, were targeted
537 for recordings. Bath application of TTX (1 µM) was performed in a subset of recorded cells to
538 verify the monosynaptic nature of the cerebellar input to zona incerta.

539 Optogenetic stimulation was delivered using a 355 nm laser (DPSS: 3505–100), controlled with
540 galvanometer mirrors (Cambridge Technology) focused on the slice through a 5x air objective
541 using custom software in MATLAB (MathWorks). Focal photostimulation of the ChR2-
542 expressing synaptic terminals in zona incerta was performed at 10Hz (4 pulses of 1-ms duration
543 at 100 ms interstimulus interval).

544 **Electrophysiological data analysis.** Electrophysiological data were collected using custom
545 MATLAB software and analyzed using Graphpad Prism (v7.0). The amplitude of excitatory
546 responses (i.e., the first response in the stimulus train) to stimulation pulses was measured by
547 subtracting the average value for 20 ms before the delivery of a pulse (baseline) from the
548 maximum value of the peak in current clamp at resting membrane potential. Latency of the
549 optogenetic response was calculated by measuring the delay in milliseconds from the onset of the
550 first optogenetic stimulus to the moment the resulting response reached >10% of its maximum
551 amplitude.

552 **Two-photon calcium imaging**

553 **Cranial window surgeries for imaging of Purkinje cell dendrites.** To minimize overall
554 recovery burden, surgeries were performed in two stages: (1) inferior olive virus injection and
555 headframe installation, and (2) cerebellar virus injection and cerebellar cranial window
556 installation as previously described[73]. In the first stage, mice (P60-90) were deeply anesthetized
557 using 1-2% isoflurane and clamped by ear bars at the external acoustic foramen. The line
558 between the clamping point and maxilla was set parallel to the horizontal plane. After trimming
559 the fur on top of the skull with clippers, the surgical site was prepared by applying betadine and
560 70% ethanol three times in an alternating fashion. Meloxicam (2 mg/kg), extended-release
561 buprenorphine (0.1 mg/kg), and 0.5 mL saline were administered subcutaneously, and depth of
562 anesthesia was confirmed via tactile stimulation of the toe before making a 20-25 mm incision in
563 the skin to reveal the occipital bone and attached tissues. After opening of the posterior atlanto-
564 occipital membrane and channelrhodopsin-2 virus injection into the left inferior olive (see
565 *Stereotaxic injections: For two-photon calcium imaging experiments*), tissues were reattached to
566 the occipital bone using instant adhesive, ensuring adequate space for later implantation of the
567 cranial window over the right cerebellar cortex. A custom titanium headframe (H. E. Parmer
568 Company, Nashville, TN, USA) was secured with dental cement (Stoelting Co., Wood Dale, IL,
569 USA), completing the first stage.

570 After monitoring recovery for a period of 4 days, mice underwent the second surgery. A circular
571 craniotomy over right cerebellar cortex with a diameter of 4mm, centered at -2.7ML; -6.9 AP,
572 was performed using a dental drill. The dura was carefully removed to expose lobules Crus I and
573 anterior Crus II before administering GCaMP6f injections (see *Stereotaxic injections: For two-*
574 *photon calcium imaging experiments*). Following injection, a two-layer glass window was
575 installed using C&B Metabond dental cement (Patterson Dental Company, Saint Paul, MN,
576 USA), completing the second stage. The glass windows consisted of a 4 mm glass window
577 (Tower Optical Corp, Boynton Beach, FL, # 4540-0495) adhered to a 5 mm glass window
578 (Warner Instruments, Holliston, MA, USA, # CS-5R) using ultraviolet light-activated glue
579 (Norland Optical Adhesive 71; Norland Products Inc., Jamesburg, NJ). Experiments were
580 conducted 4.5 weeks after inferior olive injection and 4 weeks after GCaMP6f injection.

581 **Cranial window surgeries for imaging of barrel cortex neurons.** Surgeries were again
582 separated into two stages: (1) inferior olive virus injection, headframe installation, and cerebellar
583 cranial window installation; and (2) S1 cranial window installation and virus injection. First,
584 channelrhodopsin-2 was injected into the left inferior olive as above (see *Cranial window*
585 *surgeries for imaging of Purkinje cell dendrites* and *Stereotaxic injections: For two-photon*
586 *calcium imaging*). After reattaching tissues to the occipital bone using instant adhesive, a dental

drill was used to perform a circular craniotomy over right cerebellar cortex (lobules Crus I and II), followed by removal of the dura and installation of the glass window as above. Finally, the custom titanium headframe was secured using dental cement, completing the first stage.

After monitoring recovery for a period of 4 days, mice underwent the second surgery. After surgically detaching a small portion of the left temporalis muscle attached to the parietal bone, a second circular craniotomy over left primary somatosensory cortex with a diameter of 4 mm (centered at -1.5 AP; 3 ML) was performed. The dura was removed to expose the neocortical surface before administering the appropriate viral injections (see *Stereotaxic injections: For two-photon calcium imaging experiments*). Following injection, a glass window was installed over the craniotomy using dental cement. To ensure optical isolation during recordings, a custom sheath was used to couple a Thorlabs patch cable (used for LED stimulation of cerebellar climbing fibers; see *Optogenetic and tactile stimulation*) to the cerebellar window. This sheath was adhered over the cerebellar window using Metabond dental cement, completing the second stage. For experiments involving DREADD manipulation of neurons in zona incerta, viral injections into left zona incerta were administered three days prior to the first surgery. Thus, experiments were conducted approximately 5 weeks after zona incerta injection, 4.5 weeks after inferior olive injection, and 4 weeks after primary somatosensory cortex injections.

Habituation. After completion of surgeries, postoperative care was provided for 5-7 days. Once animals exhibited exploratory behavior without signs of pain or distress, habituation began with handling of mice for 15 minutes and transportation from the animal facility to the laboratory. After two days, anxiety during handling typically diminished, and the handling period increased to 30 minutes in the vicinity of the recording area. Following two days of handling, the mice were introduced to a free-running treadmill and head restraint via clamping of the head frame on left and right sides. The duration of time spent on the treadmill increased from 10 minutes to two hours per day depending on the mouse's comfort. The relative time spent running on the treadmill typically decreased after two days. To habituate mice to air puff stimulation during this time, receptive field mapping of the field of view was conducted by delivering 8psi air puffs through a capillary tube while observing epifluorescence signals and calcium responses in real time. Air puffs were delivered at irregular frequencies, with at least 30 seconds between stimuli, to avoid influencing subsequent plasticity experiments. In total, mice were habituated for a period of 1-2 weeks until they showed no aversive responses to air puff stimulation, spent the majority of time in the recording environment at rest, and reduced movement initiation (whisking/running) with air puff stimulation. Animals used for DREADD manipulation experiments were familiarized with the DCZ injection procedure by receiving DMSO/saline injections during habituation for two days prior to recording.

Optogenetic and tactile stimulation. To optogenetically stimulate cerebellar climbing fibers, the tip of a Ø200 µm core rotary joint patch cable (Thorlabs catalog: RJPSL2) was inserted into the sheath attached to the cranial window over the right cerebellar cortex (see *Two-photon calcium imaging: Cranial window surgeries*). For experiments in which Purkinje cell responses to optogenetic climbing fiber stimulation were also measured, the patch cable was inserted into a custom light shield that fit over both the objective and the cable. The tip of the patch cable was centered over Crus II in all optogenetic stimulation experiments. Blue light pulses were delivered with a 470 nm Fiber-Coupled LED (Thorlabs catalog: M470F3). To deliver whisker stimuli, a 0.86 mm diameter glass capillary tube was positioned over the right C-row whiskers 5 mm from the right whisker pad at an angle of 45° in the X and Y planes (adjusted slightly during receptive

field mapping for each animal). Air puffs were delivered at 8 psi (Picospritzer III, Parker Hannifin). For all imaging sessions, calcium activity was measured in trials lasting 20 seconds, with a stimulus delivered once per trial. Trials began at random intervals, with an interval of at least 5 seconds between trials. When testing Purkinje cell responses to optogenetic climbing fiber stimulation, 470 nm pulses were delivered with the following durations: 1 x 20ms, 1 x 50ms, 3 x 15 ms at 8 Hz, and (3 x 15 ms at 8 Hz)*2 with a 250 ms interval between epochs. The 1 x 50 ms light pulse was selected for all subsequent experiments given this stimulation duration evoked responses resembling spontaneous events in the same Purkinje cells (Figure S1). To test the basic transmission of the climbing fiber signal to S1 (i.e., the immediate influence of optogenetic stimulation of climbing fibers on whisker responses shown in Figure 2), 100 ms air puff test pulses were delivered with or without optogenetic co-stimulation of climbing fibers. For paired test pulse stimuli, the 50 ms blue light stimulus was delivered with a delay of 45 ms with respect to the onset of the whisker stimulus. This delay was chosen to mimic the natural latency of climbing fiber responses to whisker stimulation, which peaks approximately 50 ms after stimulus onset[40]. For plasticity experiments, whisker test pulses were delivered during a baseline period of at least 30 minutes, followed by a 5-minute period of rhythmic whisker stimulation (RWS) at 8 Hz – the speed at which mice naturally sample objects[51]. For plasticity experiments with optogenetic co-activation of climbing fibers (RWS+CF), the same protocol was followed with the addition of 50 ms blue light pulses at 1 Hz during plasticity induction. The 8 Hz whisker stimulation and 1 Hz CF stimulation occurred at a consistent time relative to one another, with a blue light pulse always occurring at a 45 ms delay relative to the onset of a whisker stimulus (the same delay used for the paired test pulses). After RWS or RWS+CF, whisker test pulses were delivered for a period of at least 40 minutes. To coordinate precise stimulus delivery, a Cygnus Digital Stimulator (catalog: PG4000A, Cygnus Technology, Inc.) was interfaced with an Arduino Uno to trigger both the LED driver and picospritzer.

Cerebellar imaging protocol. Calcium imaging of the genetically encoded indicator GCaMP6f was conducted in Crus I/II of the right hemisphere of awake, head-fixed mice using a laser scanning two-photon microscope (Neurolabware, Los Angeles, CA, USA) and Scanbox software (Scanbox, Los Angeles, CA). Calcium images were obtained at a frame rate of 30.98 fps with a pixel dimension of 512 x 796, using an 8KHz resonant scanning mirror with bidirectional scanning. A Mai Tai® DeepSee (Spectra-Physics, Milpitas, CA, USA) laser source was used to excite GCaMP6f at 920 nm. The fluorescence emission was collected through a 16x water-immersion objective (Nikon LWD 0.8NA, 3 mm WD) using a GaAsP PMT (Hamamatsu Photonics, Shizuoka, Japan). A 2.0 or 2.8x digital zoom was applied during imaging, generating a field of view of 760 x 613 or 551 x 444 µm, respectively. To minimize background noise originating from ambient light, a custom light shield was fitted around the brain window and objective. This shield had a small opening such that the Thorlabs patch cable used for LED stimulation of climbing fibers could be positioned over the cerebellar window. The laser power was set to 1% with a PMT gain between 0.79 and 0.81, allowing for prolonged recording while minimizing phototoxicity.

S1 imaging protocol. Calcium imaging of GCaMP6f was conducted in barrel cortex of the left hemisphere using the same hardware as above. Images were obtained at a frame rate of 30.98 Hz with a pixel dimension of 512 x 796. A 2.4x digital zoom was applied during imaging, generating a field of view of 638 x 515 µm. Two of 11 RWS+CF experiments and one of 10 RWS experiments were conducted using a 2.0x digital zoom (generating a field of view of 760 x 613 µm) and were added to the experimental cohorts, as results were not significantly different

across any reported measures. A custom light shield was fitted around the brain window and objective to reduce background noise originating from ambient light. Note further isolation of the LED light used for optogenetic stimulation of climbing fibers in these recordings was provided by the sheath attached to the cerebellar window (see *Cranial window surgeries for imaging of barrel cortex neurons*). While observing the epifluorescence signal, small vessels on the putative surface of the brain were put into focus in the z plane and matched to a field of view selected during receptive field mapping (see *Habituation*). After adjusting the focus 250 µm below the putative pial surface, small adjustments were made in the x-y planes while observing calcium signal in real time to maximize responsivity to whisker stimulation and overlap between GCaMP6f and tdTomato or mCherry in the field of view. GCaMP6f was excited at 920 nm and tdTomato or mCherry (for DREADD experiments) at 1040 nm, with emitted fluorescence collected using two GaAsP PMTs. The laser power was set to 2%, and adjustments to the PMT gain were made due to slight variance in the level of GCaMP6f and tdTomato/mCherry signal across animals. PMT gain in the green channel was 0.73 (SD: 0.07) while PMT gain in the red channel was 0.83 (SD: 0.14), which were not significantly different across experimental groups. Responsivity to whisker stimulation was determined by intermittently delivering 8 psi air puffs at random intervals, with a minimum of 30 seconds between stimuli, to avoid influencing plasticity experiments. If more than ten minutes were spent determining an optimal field of view on the day of recording, the experiment was aborted and instead conducted the following day. Mice were occasionally used for multiple recording configurations but were sacrificed immediately after performing plasticity experiments, and selected animals were used for histological characterization (see *Tissue preparation for fluorescence microscopy and immunohistochemistry*). Note DREADD expression was histologically verified in all animals to ensure expression was restricted to neocortex.

DREADD experimental protocol. To activate the hM4D(Gi) and hM3D(Gq) receptors, we used deschloroclozapine dihydrochloride (DCZ, MedChemExpress), which was chosen over clozapine N-oxide (CNO) as an agonist due to its heightened selectivity for hM4D(Gi) and hM3D(Gq) receptors over endogenous receptors, a more rapid onset than CNO, and significantly increased potency. DCZ was dissolved in DMSO at a 0.02 mg/mL concentration and stored at −80 °C. On the day of recording, DCZ aliquots were thawed to room temperature and diluted to 0.01 mg/mL with DMSO/saline. Two-photon calcium imaging experiments began with recordings of baseline responses to whisker stimulation (with and without optogenetic stimulation of climbing fibers in a subset of experiments), followed by an injection of DCZ (0.1 mg/kg) intraperitoneally. For DREADD inhibition of PV neurons, a dose of 0.02 mg/kg was used instead, as the 0.1 mg/kg dose caused significant increases in neocortical excitability (note PV animals that had received a dose of 0.1 mg/kg were not used for any subsequent experiments or in any of the datasets shown here). Injections were carefully administered to ensure the field of view would not be disturbed; experiments were aborted if this occurred, as responses in each period could no longer be directly compared. Activation of receptors was allowed to take effect for fifteen minutes prior to resumption of recording, after which a second period of baseline activity was recorded. This period lasted between fifteen and thirty minutes, such that a period of fifteen minutes of stable activity was recorded prior to plasticity induction. Plasticity induction protocols were followed as above (see *Optogenetic and tactile stimulation*), and whisker test pulses were delivered for at least 40 minutes after plasticity induction. To ensure observed plasticity phenomena were not the result of prolonged changes in activity related to hM4D(Gi) or hM4D(Gq) activation, control experiments lasting the same duration as the plasticity

experiments were conducted similarly, except without induction of plasticity (see Figure S5). To ensure DREADD expression was localized to the neocortex, viral spread was histologically characterized in all animals (see *Tissue preparation for fluorescence microscopy and immunohistochemistry*).

Characterization of neurons. Calcium images taken in the green (PMT0) and red (PMT1) channels were first merged, trial-averaged, and concatenated using Fiji. The average image was then calculated, followed by identification of all cells expressing tdTomato or mCherry (applicable to all recordings except the zona incerta manipulation experiments). ROIs were manually drawn around each cell co-expressing GCaMP6f and tdTomato or mCherry. All images across a session were then concatenated and trial-averaged before calculating the maximum image. ROIs were manually drawn around all putative pyramidal neurons, which were identified with the following criteria: a triangular or pyramidal soma, the presence of a single apical dendrite extending in a similar orientation to other pyramidal cells in the same imaging session, and the presence of basal dendrites smaller in diameter than the apical dendrite. In a subset of experiments in which apical dendrites could not be clearly distinguished in the imaging plane, z-stack images were taken at the end of the imaging session, averaged, and referenced to visualize apical dendrites. After identification of fluorescently tagged interneurons and pyramidal neurons, relevant putative interneurons were morphologically identified and compiled (e.g., putative VIP and SST neurons in PV-tagged mice). Putative interneurons were identified by the presence of an elongated soma and bipolar dendritic arbors (likely VIP), round somas smaller in diameter than pyramidal cells, and neurons with multiple perisomatic dendrites (usually highly branched; likely PV). The morphology of untagged interneurons was visually compared to the morphology of tagged interneurons in relevant mice (e.g., morphologically identified interneurons in PVCre mice were compared to fluorescently tagged interneurons in SSTCre and VIPCre mice). The average (11.07µm, SD 1.64µm) and maximum (18.14µm, SD 2.74µm) soma diameter for morphologically identified pyramidal neurons ($n = 3358$) were significantly higher than in morphologically identified interneurons in the same mice ($n = 3522$; average: 9.90µm, SD 1.96; maximum: 16.37µm, SD: 3.39µm; $p < 0.001$ for both values, unpaired t-test) and tagged VIP, SST, and PV neurons ($n = 543$; average: 8.96µm, SD 1.87µm; maximum: 14.98µm, SD 3.51µm; $p < 0.001$ for both values, unpaired t-test).

Intrinsic Signal Imaging

Image acquisition. Mice underwent the same surgical procedures described in *Two-Photon calcium imaging: Cranial window surgeries for imaging of barrel cortex neurons.* To facilitate manipulation of single whiskers, mice were lightly anesthetized with 10 mg/kg ketamine and placed on a stereotaxic frame. Using a custom GUI written in MATLAB, small vessels were visualized under a green LED (525 nm wavelength) with a high-speed camera (Teledyne DALSA Genie Nano GigE). Focus in the z-plane was adjusted approximately 250 µm below the putative pial surface before taking a reference image of the vasculature. For measurement of intrinsic signals, the field of view was illuminated with red light (625 nm). An Arduino Uno and MATLAB were used to trigger trial onset, the device used to mechanically deflect whiskers (a glass capillary tube attached to a rotary motor), a blue LED to stimulate climbing fibers, and recording of intrinsic signals at 30 Hz. Trials consisted of a 1-second baseline period, followed by a 1-second test pulse in which whiskers contralateral to the optical window were mechanically deflected at 8 Hz (RWS). This was repeated with an inter-trial interval of 18

seconds for 30 minutes prior to plasticity induction, after which whiskers were stimulated at 8 Hz for 5 minutes. Test pulses were delivered for 40 minutes after plasticity induction. For RWS+CF and control experiments, 50 ms blue light pulses were delivered at 1 Hz during plasticity induction with or without 8 Hz co-stimulation of whiskers, respectively.

Image processing. Evoked signals were calculated similarly to Vasquez *et al* [94]. Briefly, images were smoothed with a Gaussian filter and spatially downsampled by a factor of four. For each trial, an average baseline reflectance image (R0) was generated by calculating the average across the 1-second (30 frame) period before stimulus onset. Post-stimulus reflectance images were temporally averaged across 200 ms bins for 600 ms total, starting 400 ms after stimulus onset. The change in reflectance, ΔR/R, was calculated by subtracting R0 from each post-stimulus image and dividing the result by R0. Each of the three bins (400-600 ms, 600-800 ms, and 800 ms-1 s post stimulus onset) were averaged across a minimum of 30 trials and finally summed to yield a single total stimulus-evoked ΔR/R image. The reference image taken with green light illumination was used to draw a region of interest around the cranial window. Pixels outside this ROI mask were set to zero. Binary images were generated by calculating z-scores of the ΔR/R image and thresholding values below a z-score of -1.5 (note negative changes in reflectance indicate an increase in the presence of deoxyhemoglobin caused by increased oxygen consumption by active neurons). Binarized images were overlaid onto reference images. To calculate the areal extent of single whisker-evoked responses, clusters of active pixels were identified by applying a median filter with a 5 x 5-pixel neighborhood size, and the number of pixels above threshold was calculated. To reduce the impact of residual noise (i.e. detected pixels outside the area reliably activated by a single whisker), values were normalized by the area of the cranial window.

Two-photon image processing

Processing of cerebellar data. Processing of Purkinje cell calcium traces was conducted as previously described[23, 73]. Individual trials from each session were concatenated along the z-axis, representing a time series across the entire recording session, to ensure consistency among trials after motion correction. The concatenated file underwent motion correction using a custom MATLAB script (MATLAB R2017b, MathWorks, Natick, MA, USA) based on whole frame cross-correlation (provided by the lab of Mark Sheffield, University of Chicago). Cellular regions of interest were manually selected in Fiji based on the average field of view across trials. Trials were then separated for further processing. In a subset of trials, optogenetic stimulus artifacts were visible in a portion of the field of view in 1-3 nonconsecutive frames, depending on the stimulus duration. These frames were manually identified and excluded using Fiji before further processing.

Using custom MATLAB script, ΔF/F values were calculated from the raw trace using the following equation: $(Ft - F0)/F0$, where Ft represented the raw calcium intensity of the time series, and the baseline fluorescence (F0) was set as the 20th percentile of the fluorescence trace from each trial. ΔF/F values were then subjected to low-pass filtering using a five-frame moving window smoothing function. Finally, traces were normalized to a pre-stimulus baseline period by subtracting the average ΔF/F value from the 5-frame period prior to stimulus onset from the entire trace. To visualize population average responses to optogenetic stimulation of climbing fibers, calcium signals from each ROI were first trial-averaged, followed by concatenation and

averaging of the signal across cells and mice. To calculate maximum amplitude of responses in the evoked period, the maximum in a window 0-700 ms after stimulus onset was calculated for each ROI's trial-averaged trace, then concatenated across cells and mice. Area under the curve (AUC) was calculated similarly by integrating the ΔF/F values over the same window. To identify spontaneous events, frame indices in which the first and second derivatives of the ΔF/F signal reached 0.04 were identified (F^{idx}). Peaks were detected using a peak prominence threshold of 0.1 ΔF/F, with spontaneous events defined as peaks occurring within 200 ms of F^{idx}. The onset of each spontaneous event was determined as the first frame in which the first derivative of the ΔF/F dropped below 0.05 (working backward from frame index of the detected peak). A 1-second window following event onset was extracted. Finally, after averaging all detected spontaneous events within ROIs, spontaneous events were compiled across neurons to generate the population average trace.

Processing of S1 data. Motion correction and ROI curation were performed as above (see *Processing of cerebellar data* and *Two-photon calcium imaging: Characterization of neurons*). Residual optogenetic stimulus artifacts were observed in a single frame in a subset of trials, typically at or immediately after stimulus offset. These artifacts were detected using the *findpeaks* function in MATLAB and corrected by replacing the artifact frame's value with a linear interpolation of the two adjacent frames before further processing. Background subtraction was performed by calculating the bottom 1st percentile of the raw fluorescence trace collected from an ROI that did not contain cell bodies or neuropil, then subtracting this value from all trials. Smoothing, expression of raw signals as ΔF/F, calculation of baseline noise (σ), and calculation of the signal-to-noise ratio (SNR) were performed as in Ayaz *et. al.*[95]. Smoothing was performed with a 51-point 1st-order Savitsky-Golay filter, followed by calculation of the relative percent change of fluorescence ($(F_t - F_0)/F_0$) using the 1st percentile of the smoothed trace as F0. Given background subtraction prior to calculation of F0 may generate negative F0 values and subsequent signal inversion, ROIs with $F_0 < 0$ were rejected from further analyses (44/7423 cells). To calculate σ for each neuron, a 5-second (155 frame) sliding window was first used to calculate the standard deviation of the fluorescence change during each 5-second period within a session. After compiling all values, the 1st percentile value was taken as σ. For each neuron, the SNR was defined as the 95th percentile of ΔF/F signals recorded across all trials divided by the baseline noise.

Evoked event detection. To detect whisker–evoked events, we first applied OASIS deconvolution to the ΔF/F traces using an event detection threshold of 3σ to generate a binary trace containing event times. An autoregressive model with order p=1 was used to ensure the number of events ("spikes") for each calcium transient varied with the amplitude of the calcium transient as previously observed[52]. Next, for each frame, the sum of all events was calculated and divided by the number of trials to determine the proportion of trials with an event in a given frame (P^{event}). P^{event} was averaged across frames, and consecutive frames with P^{event} 3 standard deviations above the mean were selected. This generated an evoked event window of 387 ms (Supplementary Data 2B). Finally, for each neuron, the calcium traces for all trials containing an event within the evoked event window were compiled for further analysis. To visualize population average traces for all experiments, evoked calcium signals for each neuron were first averaged across trials, followed by averaging across neurons. For visualizations between the same neural populations in different conditions, only those cells that responded to both conditions, i.e. having an evoked event in each condition, were included (following the definition

856 of "Persistent cells" used in Williams *et. al.*[60]). Shaded regions in population average traces
857 represent SEM.

858 **Calculation of amplitude and area under the curve in S1 recordings.** For all calculations of
859 AUC in S1 recordings, the ΔF/F signal was integrated over a 700 ms window after stimulus
860 onset unless otherwise specified (details below).

861 To quantify plasticity phenomena caused by RWS or RWS+CF, all evoked events measured
862 within 50 minutes prior to plasticity induction ("Pre") or 60 minutes after plasticity induction
863 ("Post") were extracted for each cell and trial-averaged before calculating AUC. Only the
864 neurons with evoked events both pre- and post-plasticity induction were included in subsequent
865 analyses. AUC were averaged both across all neurons or within animal to perform statistics
866 across neurons or mice (see *Statistics and quantifications*). To visualize the duration of plasticity
867 effects, evoked events were binned into 10-minute epochs and trial-averaged within cells,
868 followed by calculation of the AUC and averaging across neurons. To verify the robustness of
869 plasticity effects, AUC and time course measurements were also analyzed across all cells and
870 trials (i.e., those that did not have stimulus-evoked events; Figure S2) and in the absence of
871 animal movement (Figure S3; see *Determination of active and rest trials*). To quantify plasticity
872 phenomena in DREADD manipulation experiments, response amplitude was calculated in
873 addition to AUC before and after plasticity induction. Response amplitude was taken as the
874 maximum ΔF/F value in the same 700 ms window used for AUC calculations.

875 To quantify the immediate effect of climbing fiber activation on basic whisker responses in S1
876 cortex, AUC was calculated similarly for whisker stimulation (W) or whisker and CF co-
877 activation (W+CF) trials. An additional measurement was taken 650-850 ms after stimulus onset
878 for pyramidal neurons and VIP interneurons, as the effect of CF modulation was present in the
879 later phase of the calcium response. Note that while W and W+CF test pulses were delivered
880 prior to DCZ administration in DREADD experiments to verify functional opsin expression,
881 these mice were excluded from this analysis due to an insufficient number of trials in each
882 animal.

883 To verify that hM4D(Gi) and hM3D(Gq) expression in SST neurons indeed suppressed or
884 increased their activity, respectively, AUC was calculated before and after DCZ administration
885 in a window 1750 ms after stimulus onset. This larger window was used to capture the
886 significantly increased duration of whisker-evoked calcium responses in SST neurons expressing
887 hM3D(Gq). To verify that hM4D(Gi) and hM3D(Gq) expression in VIP neurons indeed
888 suppressed or increased their activity, respectively, AUC was calculated before and after DCZ
889 administration in a window 650-850 ms after stimulus onset. Given VIP neurons are modulated
890 by climbing fiber stimulation in this phase of the calcium response (Figure 2g), this later window
891 was chosen to ensure DREADD manipulation of VIP neurons suppressed or enhanced VIP
892 responses in the physiologically relevant response period.

893 **<u>Determination of active and rest trials</u>**

894 Activity of mice was monitored at 30.98 Hz using a DALSA M640 CCD camera (Teledyne
895 Technologies, Thousand Oaks, CA, USA) focused on the animal's face and a portion of the
896 running wheel. To determine the frames in which mice were active, custom MATLAB script was
897 used to generate a binary trace that indicated the frames in which movement between frames

occurred (based on a comparison of pixel values between consecutive frames). For each recording session, movement traces and corresponding videos from ten randomly selected trials were manually inspected to ensure all frames in which mice were whisking or running were indicated. Note whisking occurred independently of running, but running seldom occurred without whisking. Rest trials were defined as any trial with no movement detected at least 400 ms before and after stimulus onset – longer than the evoked event window, and the same as the window chosen in Ayaz *et. al.*[95] to distinguish rest from running onset. All other trials were considered active trials.

Statistics and quantifications

All statistics and quantifications were performed using MATLAB. To assess normality, we applied the Lilliefors test to each dataset before performing statistical calculations. For paired samples, a paired t-test was used when data were normally distributed, and a Wilcoxon signed-rank test was used for non-normal data. For unpaired comparisons, an unpaired t-test was used for normally distributed data, a Welch's t-test for normally distributed data with unequal variances, and a Wilcoxon rank-sum test for non-normal distributions. Categorical variables were compared using the Chi-squared test. Two-way ANOVA was used for multi-group comparisons (i.e., to determine whether plasticity effects across time were significantly different between groups). To perform statistics across all animals, average responses were first normalized by dividing the response in the relevant experimental condition by the baseline response. A one-sample t-test was then performed against a standard value of 1. Statistical significance was set to $p < 0.05$, with p values presented in figures as follows: $p < 0.05$: *; $p < 0.01$: **; $p < 0.001$: ***; $p > 0.05$: not significant (n.s.). Bar graphs represent mean ± SEM. Box plots contain the interquartile range (25th and 75th percentiles) and median.

Resource availability

Lead contact

Further information and requests for resources and reagents should be directed and will be fulfilled by the lead contact, Christian Hansel (chansel@bsd.uchicaho.edu).

Data availability

All data shown here, as well as additional two-photon and confocal imaging data described in the Methods, will be placed on GitHub prior to publication.

Code availability

All code used for the analyses will be provided prior to publication, with accession codes made available for public access.

Acknowledgements

We thank Drs. M. Brecht (Humboldt University, Berlin) as well as A.M. Oswald and S.M. Sherman (both University of Chicago) for invaluable feedback on the manuscript. We thank S.R. Postlewaite and current and former Hansel lab members S.E. Busch, D. Huang and T.F. Lin for insightful discussions and comments on the manuscript. This work was supported by National Institutes of Health (NINDS) grants R21NS136954 (to C.H.) and NS094184 (to K.P.K. in the lab

of S.M. Sherman).

Declaration of Interests

The authors declare no competing interests.

References

1. K. Doya, Complementary r.oles of basal ganglia and cerebellum in learning and motor control. *Curr. Opin. Neurobiol*. **10**, 732-739 (2000).
2. M. E. Diamond, M. Armstrong-James, F. F. Ebner, Experience-dependent plasticity in adult rat barrel cortex. *Proc. Natl. Acad. Sci. USA* **90**, 2082-2086 (1993). Doi:10.1073/pnas.905.2082.
3. S. Glazewski, A. L. Barth, H. Wallace, M. McKenna, A. Silva, K. Fox, Impaired experience-dependent plasticity in barrel cortex of mice lacking the alpha and delta isoforms of CREB. Cereb. Cortex **9**, 249-256 (1999).
4. E.A. Stern, M. Maravall, K. Svoboda, Rapid development and plasticity of layer 2/3 maps in rat barrel cortex in vivo. *Neuron* **31**, 305-315 (2001). Doi: 10.1016/s0896-6273(01)00360-9.
5. J. Delacour, O. Houcine, J. C. Costa, Modifications of the responses of barrel field neurons to vibrissal stimulation during theta in the awake and undrugged rat. *Neuroscience* **37**, 237-243 (1990).
6. P. Megevand, E. Troncoso, C. Quairiaux, D. Muller, C. M. Michel, J. Z. Kiss, Long-term plasticity in mouse sensorimotor circuits after rhythmic whisker stimulation. *J. Neurosci*. **29**, 5326-5335 (2009).
7. F. Gambino, S. Pages, V. Kehayas, D. Baptista, R. Tatti, A. Carleton, A. Holtmaat, Sensory-evoked LTP driven by dendritic plateau potentials in vivo. *Nature* **515**, 116-119 (2014).
8. D. E. Feldman, Timing-based LTP and LTD at vertical inputs to layer II/III pyramidal cells in rat barrel cortex. *Neuron* **27**, 45-56 (2000).
9. L. E. Williams, A. Holtmaat, Higher-order thalamocortical inputs gate synaptic long-term potentiation via disinhibition. *Neuron* **101**, 91-102 (2019).
10. D. E. Feldman, M. Brecht, Map plasticity in somatosensory cortex. *Science* **310**, 810-815 (2005).
11. J. D. Schmahmann, J. C. Sherman, The cerebellar cognitive affective syndrome. *Brain* **121**, 561-579 (1998).
12. C. J. Stoodley, P. T. Tsai, Adaptive prediction for social contexts: the cerebellar contribution to typical and atypical social behaviors. *Annu. Rev. Neurosci*. **44**, 475-493 (2021).
13. F. A. Middleton and P. L. Strick, Cerebellar projections to the prefrontal cortex of the primate. *J. Neurosci*. **21**, 700-712 (2001).
14. P. L. Strick, R. P. Dum, J. A. Fiez, Cerebellum and non-motor function. *Annu. Rev. Neurosci*., **32**, 413-434 (2009).
15. A. Badura, J. L. Verpeut, J. W. Metzger, T. D. Pereira, T. J. Pisano, B. Deverett, D. E. Bakshinskaya, S. S. Wang, Normal cognitive and social development require posterior cerebellar activity. *eLife* **7**, e36401 (2018).
16. E. Kelly et al., Regulation of autism-relevant behaviors by cerebellar-prefrontal cortical circuits. *Nat. Neurosci*. **23**, 1102-1110 (2020).
17. T. J. Pisano et al., Homologous organization of cerebellar pathways to sensory, motor, and associative forebrain. *Cell Rep*. **36**, 109721 (2021).

18. Z. Gao, C. Davis, A.M. Thomas, M.N. Economo, A.M. Abrego, K. Svoboda, C.I. De Zeeuw, N. Li. A cortico-cerebellar loop for motor planning. *Nature* **563**, 113-116.

19. D. Popa, M. Spolidoro, R. D. Proville, N. Guyon, L. Belliveau, C. Lena, Functional role of the cerebellum in gamma-band synchronization of the sensory and motor cortices. *J. Neurosci*. **33**, 6552-6556 (2013).

20. S. McAfee, Y. Liu, R. V. Sillitoe, D. H. Heck, Cerebellar lobulus simplex and Crus I differentially represent phase and phase difference of prefrontal cortical and hippocampal oscillations. *Cell Rep*. **27**, 2328-2334 (2019).

21. S. Lindeman, S. Hong, L. Kros, J. F. Mejias, V. Romano, R. Oostenveld, M. Negrello, L. W. Bosman, C. I. De Zeeuw, Cerebellar Purkinje cells can differentially modulate coherence between sensory and motor cortex depending on region and behavior. *Proc. Natl. Acad. Sci. USA* **118**, e2015292118 (2021).

22. E. R. Goldenkoff, J.A. Brissenden, T.G. Lee, K.J. Michon, M. Vesia. Cerebellar activity affects distal cortical physiology and synaptic plasticity in a human parietal-motor pathway associated with motor actions. *J. Neurosci*. **45**, e0404252025.

23. S. E. Busch, C. Hansel, Climbing fiber multi-innervation of mouse Purkinje dendrites with arborization common to human. *Science* **381**, 420-427 (2023).

24. D. Marr, A theory of cerebellar cortex. *J. Physiol*. **202**, 437-470 (1969).

25. J. S. Albus, A theory of cerebellar function. *Math. Biosci*. **10**, 25-61 (1971).

26. M. Ito, M. Yoshida. The cerebellar-evoked monosynaptic inhibition of Deiters' neurons. *Experientia* **20**, 515-516 (1964).

27. M. Ito, M. Kano, Long-lasting depression of parallel fiber-Purkinje cell transmission induced by conjunctive activation of parallel fibers and climbing fibers in the cerebellar cortex. *Neurosci. Lett*. **33**, 253-258 (1982).

28. M. Ito, M. Sakurai, P. Tongroach, Climbing fibre induced depression of both mossy fibre responsiveness and glutamate sensitivity of cerebellar Purkinje cells. *J. Physiol*. **265**, 833-854 (1982).

29. S. S. Wang, W. Denk, M. Häusser, Coincidence detection in single dendritic spines mediated by calcium release. *Nat. Neurosci*. **3**, 1266-1273 (2000).

30. V. Lev-Ram, S. T. Wong, D. R. Storm, R. Y. Tsien, A new form of cerebellar potentiation is postsynaptic and depends on nitric oxide but not cAMP. *Proc. Natl. Acad. Sci. USA* **99**, 8389-8393 (2002).

31. M. Coesmans, J. T. Weber, C. I. De Zeeuw, C. Hansel, Bidirectional parallel fiber plasticity in the cerebellum under climbing fiber control. *Neuron* **44**, 691-700 (2004).

32. C. Piochon, H. K. Titley, D. H. Simmons, G. Grasselli, Y. Elgersma, C. Hansel, Calcium threshold shift enables frequency-independent control of plasticity by an instructive signal. *Proc. Natl. Acad. Sci. USA* **113**, 13221-13226 (2016).

33. A. Suvrathan, H. L. Payne, J. L. Raymond, Timing rules for synaptic plasticity matched to behavioral function. *Neuron* **92**, 959-967 (2016).

34. H. K. Titley, M. Kislin, D. H. Simmons, S. S. Wang, C. Hansel, Complex spike clusters and false-positive rejection in a cerebellar supervised learning rule. *J. Physiol*. **597.16**, 4387-4406 (2019).

35. J. F. Medina, J. C. Repa, M. D. Mauk, J. E. LeDoux, Parallels between cerebellum- and amygdala-dependent conditioning. *Nat. Rev. Neurosci*. **3**, 122-131 (2002).

36. Y. Yang, S. G. Lisberger, Interaction of plasticity and circuit organization during the acquisition of cerebellum-dependent motor learning. *eLife* **2**, e01574 (2013).

37. Y. Yang, S. G. Lisberger, Purkinje-cell plasticity and cerebellar motor learning are graded by complex-spike duration. *Nature* **510**, 529-532 (2014).

38. N. T. Silva, J. Ramirez-Buritica, D. L. Pritchett, M. R. Carey, Climbing fibers provide essential instructive signals for associative learning. *Nat. Neurosci*. **27**, 940-951 (2024).

39. J. I. Simpson, D. R. Wylie, C. I. De Zeeuw, On climbing fiber signals and their consequence(s). *Behav. Brain Sci*. **19**, 384-398 (1996).

40. L. W. Bosman et al., Encoding of whisker input by cerebellar Purkinje cells. *J. Physiol*. **588**, 3757-3783 (2010).

41. D. J. Herzfeld, R. Shadmehr, Cerebellum estimates the sensory state of the body. *Trends Cogn. Neurosci*. **18**, 66-67 (2014).

42. F. Najafi, A. Giovannucci, S. S. Wang, J. F. Medina, Sensory-driven enhancement of calcium signals in individual Purkinje dendrites of awake mice. *Cell Rep*. **6**, 792-798 (2014a).

43. F. Najafi, A. Giovannucci, S. S. Wang, J. F. Medina, Coding of stimulus strength via analog calcium signals in Purkinje cell dendrites of awake mice. *eLife* **3**, e03663 (2014b).

44. M. A. Gaffield, A. Bonnan, J. M. Christie, Conversion of graded presynaptic climbing fiber activity into graded postsynaptic Ca2+ signals by Purkinje cell dendrites. *Neuron* **102**, 762-769 (2019).

45. S. Ohmae, J. F. Medina, Climbing fibers encode a temporal-difference prediction error during cerebellar learning in mice. *Nat. Neurosci*. **18**, 1798-1803 (2015).

46. W. Heffley, C. Hull, Classical conditioning drives learned reward prediction signals in climbing fibers across the lateral cerebellum. *eLife* **8**, e46764 (2019).

47. D. Kostadinov, M. Beau, M. Blano-Pozo, M. Häusser, Predictive and reactive reward signals conveyed by climbing fiber inputs to cerebellar Purkinje cells. *Nat. Neurosci*. **22**, 950-962 (2019).

48. D. H. Simmons, S. E. Busch, H. K. Titley, G. Grasselli, J. Shi, X. Du, C. Wei, C. M. Gomez, C. Piochon, C. Hansel, Sensory over-responsivity and aberrant plasticity in cerebellar cortex in a mouse model of syndromic autism. *Biol. Psychiatry: GOS* **2**, 450-459 (2022).

49. J. S. Jouhanneau, L. Ferrarese, L. Estebanez, N. J. Audette, M. Brecht, A. L. Barth, J. F. Poulet, Cortical fosGFP expression reveals broad receptive field excitatory neurons targeted by Pom. *Neuron* **84**, 1065-1078 (2014).

50. N. J. Audette, S. M. Bernhard, A. Ray, L. T. Stewart, A. L. Barth, Rapid plasticity of higher-order thalamocortical inputs during sensory learning. *Neuron* **103**, 277-291 (2019).

51. M. E. Diamond, M. von Heimendahl, P. M. Knutsen, D. Kleinfeld, E. Ahissar, 'Where' and 'what' in the whisker sensorimotor system. *Nature Rev. Neurosci*. **9**, 601-612 (2008).

52. L. Theis et al., Benchmarking spike rate inference in population calcium imaging. *Neuron* **90**, 471-482 (2016).

53. M. Brecht, A. Roth, B. Sakmann, Dynamic receptive fields of reconstructed pyramidal cells in layers 2 and 3 of rat somatosensory barrel cortex. *J. Physiol*. **553**, 243-265 (2003).

54. J. Heiss, Y. Katz, E. Ganmor, I. Lampl, Shift in the balance between excitation and inhibition during sensory adaptation of S1 neurons. *J. Neurosci.* **28**, 13320-13330 (2008).

55. J.F. Staiger, C.C.H. Petersen, Neuronal circuits in barrel cortex for whisker sensory perception. *Physiol. Rev*. **101**, 353-415 (2021).

56. R. Tremblay, S. Lee, B. Rudy, GABAergic interneurons in the neocortex: from cellular properties to circuits. *Neuron* **91**, 260-292 (2016).

57. T. Bonhoeffer, A. Grinvald, Iso-orientation domains in cat visual cortex are arranged in pinwheel-like patterns. *Nature* **353**, 429-431 (1991).

58. B. S. Sermet, P. Truschow, M. Feyerabend, J. M. Mayrhofer, T. B. Oram, O. Yizhar, J. F. Staiger, C. C. H. Petersen, Pathway- layer- and cell-type-specific thalamic input to mouse barrel cortex. *eLife* **8**, e52665 (2019).

59. N. J. Audette, J. Urban-Cieko, M. Matsushita, A. L. Barth, POm thalamocortical input drives layer-specific microcircuits in somatosensory cortex. *Cereb. Cortex* **28**, 1312-1328 (2018).

60. L. E. Williams, L. Küffer, T. Bawa, E. Husi, S. Pagès, A. Holtmaat, Repetitive sensory stimulation potentiates and recruits sensory-evoked cortical population activity. *J. Neurosci*. **45**, e2189232024 (2025).

61. M. Novello, L.W. Bosman, C. I. De Zeeuw, A systematic review of direct outputs from the cerebellum to the brainstem and diencephalon in mammals. *Cerebellum* **23**, 210-239 (2022).

62. Y. Zhao, J. Wu, J. Feng, X. Cai, X. Wang, L. Wang, W. Xie, Y. Gu, J. Liu, W. Chen, L. Zhou, Y. Shen, Dual and plasticity-dependent regulation of cerebello-zona incerta circuits on anxiety-like behaviors. *Nature Comm.* **16***,* 3339 (2025).

63. P. Bartho, T. F. Freund, L. Acsady, Selective GABAergic innervation of thalamic nuclei from zona incerta. *Eur. J. Neurosci*. **16**, 999-1014 (2002).

64. R. I. Martinez-Garcia, B. Voelcker, J. B. Zaltsman, S. L. Patrick, T. R. Stevens, B.W. Connors, S. J. Cruikshank, Two dynamically distinct circuits driving inhibition in sensory thalamus. *Nature* **22**, 813-818 (2020).

65. B. Zingg, X.L. Chou, Z.G. Zhang, L. Mesik, F. Liang, H.W. Tao, L.I. Zhang, AAV-mediated anterograde transsynaptic tagging: mapping corticocollicular input-defined neural pathways for defense behaviors. *Neuron* **93**, 33-47 (2017).

66. J.H. Cho, K. Deisseroth, V.Y. Bolshakov, Synaptic encoding of fear extinction in mPFC-amygdala circuits. *Neuron* **80**, 1491-1507 (2013).

67. J. C. Trageser, K. A. Burke, R. Masri, Y. Li, L. Sellers, A. Keller, State-dependent gating of sensory inputs by zona incerta. *J. Neurophysiol*. **96**, 1456-1463 (2006).

68. M. Zhu, S. J. Kuhlman, A. L. Barth, Transient enhancement of stimulus-evoked activity in neocortex during sensory learning. *Learn. Mem*. **31**, a053870.123 (2024).

69. J.M. Bower, Is the cerebellum sensory for motor's sake or motor for sensory's sake: the view from the whiskers of a rat? *Prog. Brain Res*. 114, 483-516 (1997).

70. O. Baumann et al., Consensus paper: the role of the cerebellum in perceptual processes. *Cerebellum* 14, 197-220 (2015).

71. L.W. Bosman et al., Anatomical pathways involved in generating and sensing rhythmic whisker movements. *Front. Integr. Neurosci*. **5**, 53 (2011).

72. K.B. Ramakrishnan, K. Voges, L. De Propris, C.I. De Zeeuw, E. D'Angelo, Tactile stimulation evokes long-lasting potentiation of Purkinje cell discharge in vivo. *Front. Cell. Neurosci*. **10**, 36 (2016).

73. T.F. Lin, S.E. Busch, C. Hansel, Intrinsic and synaptic determinants of receptive field plasticity in Purkinje cells of the mouse cerebellum. *Nat. Commun*. **15**, 4645 (2024).

74. J. P. Welsh, Functional significance of climbing-fiber synchrony. A population coding and behavioral analysis. *Ann. N. Y. Acad. Sci*. **978**, 188-204 (2002).

75. S. Kitazawa, D. M. Wolpert, Rhythmicity, randomness and synchrony in climbing fiber signals. *Trends Neurosci*. **28**, 611-619 (2005).

76. S. R. Schultz, K. Kitamura, A. Post-Uiterweer, J. Krupic, M. Häusser, Spatial pattern coding of sensory information by climbing fiber-evoked calcium signals in networks of neighboring cerebellar Purkinje cells. *J. Neurosci*. **29**, 8005-8015 (2009).

77. V. Gauck, D. Jaeger, The control of rate and timing of spikes in the deep cerebellar nuclei by inhibition. *J. Neurosci*. **20**, 3006-3016 (2000).

78. A. L. Person, I. M. Raman, Purkinje neuron synchrony elicits time-locked spiking in the cerebellar nuclei. *Nature* **481**, 502-506 (2012).

79. T. Tang, T.A. Blenkinsop, E.J. Lang, Complex spike synchrony dependent modulation of rat deep cerebellar nuclear activity. *eLife* **8**, e40101 (2019).

80. D. Feldmeyer, M. Brecht, F. Helmchen, C.C.H. Petersen, J. F. Poulet, J. F. Staiger, H. J. Luhmann, C. Schwarz, Barrel cortex formation. *Prog. Neurobiol*. **103**, 3-27 (2013).

81. Y. Ugawa, B.L. Day, J.C. Rothwell, P.D. Thompson, P.A. Merton, C.D. Marsden. Modulation of motor cortical excitability by electrical stimulation over the cerebellum in man. *J. Physiology.* **441**, 57-72 (1991).

82. Y. Ugawa, Y. Uesaka, Y. Terao, R.H. Hanajima, I. Kanazawa. Magnetic stimulation over the cerebellum in humans. *Ann. Neurology* **37**, 691-821 (1995).

83. J. Ge et al., Ventral zona incerta parvalbumin neurons modulate sensory-induced and stress-induced self-grooming via input-dependent mechanisms in mice. *iScience* **27**, 110165 (2024).

84. J. M. Kebschull et al. Cerebellar nuclei evolved by repeatedly duplicating a conserved cell-type set. *Science* **370**, eabd5059 (2020).

85. J. Beckinghausen et al. The cerebellum contributes to generalized seizures by altering activity in the ventral posteromedial nucleus. *Comm. Biol*. **6**, 731 (2023).

86. T. Mao, D. Kusefoglu, B.M. Hooks, D. Huber, L. Petreanu, K. Svoboda. Long-range neuronal circuits underlying the interaction between sensory and motor cortex. *Neuron* **72**, 111-132 (2011).

87. S. Lee, I. Krugilov, Z.J. Huang, G. Fishell, B. Rudy. A disinhibitory circuit mediates motor integration in the somatosensory cortex. *Nat. Neurosci*. **11**, 1662-1670 (2013).

88. E. I. Knudsen, Supervised learning in the brain. *J. Neurosci*. **14**, 3985-3997 (1994).

89. C. Viollet, A. Simon, V. Tolle, A. Labarthe, D. Grouselle, Y. Loe-Mie, M. Simonneau, G. Martel, J. Epelbaum. Somatostatin-IRES-Cre Mice: Between Knockout and Wild-Type? *Front Endocrinol* **8** (2017).

90. A. H. Cheng, S. W. Fung, H. M. Cheng. Limitations of the Avp-IRES2-Cre (JAX #023530) and Vip-IRES-Cre (JAX #010908) Models for Chronobiological Investigations. *J Biol Rhythms* **34**, 634-644 (2019).

91. K. P. Koster, S. M. Sherman. Convergence of inputs from the basal ganglia with layer 5 of motor cortex and cerebellum in mouse motor thalamus. *eLife* **13**, e97489 (2024).

92. G. Paxinos, K. B. J. Franklin. *Paxinos and Franklin's The Mouse Brain in Stereotaxic Coordinates* (Elsevier, ed. 5, 2019).

93. T. Miyazaki, M. Watanabe. Development of an anatomical technique for visualizing the mode of climbing fiber innervation in Purkinje cells and its application to mutant mice lacking GluRδ2 and Ca(v)2.1. *Anat Sci Int* **86 (**2011).

94. B. Vasquez, B. Campos, A. Cao, A. T. Theint, W. Zeiger. High-Sensitivity Intrinsic Optical Signal Imaging Through Flexible, Low-Cost Adaptations of an Upright Microscope. *eNeuro* **10** (2023).

95. A. Ayaz, A. Stäuble, M. Hamada, M. A. Wulf, A. B. Saleem, F. Helmchen. Layer-specific integration of locomotion and sensory information in mouse barrel cortex. *Nature Commun* **10**, 2585 (2019).

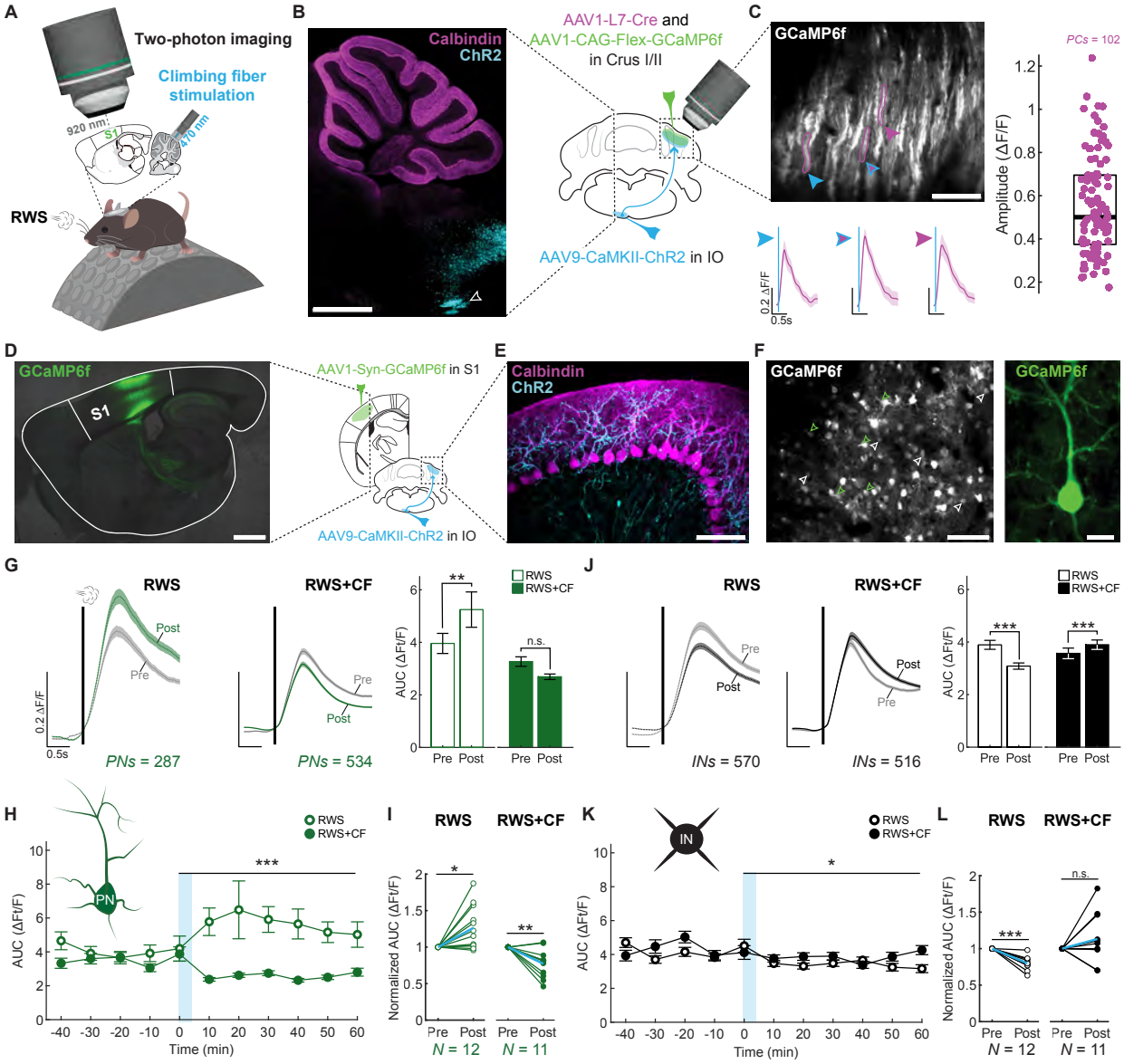

Figure 1. Optogenetic CF co-activation prevents adaptive L2/3 pyramidal cell potentiation in S1 cortex. (**A**) Experimental schematic for (**D** – **L**). (**B** and **C**) ChR2 expression in the inferior olive (IO) and optogenetic CF activation evokes calcium transients in PCs. (**B**) Calbindin staining of PCs marks the cerebellum (shown here in the same plane as the IO; white arrowhead). Scale bar: 1mm. (**C**) Top view of PC dendrites with calcium responses evoked by 470nm, 50ms LED pulses in PCs. Scale bar: 100µm. Right: Distribution of response amplitudes (box: 25th and 75th percentiles; line: median). (**D**) GCaMP6f expression in S1 cortex. Scale bar: 1mm. (**E**) Sagittal view of ChR2-expressing CF terminals in cerebellum that are activated in optogenetic experiments. Scale bar: 100µm. (**F**) Left: Example of the morphological identification of L2/3 pyramidal cells by apical dendrites (green arrowheads) and INs (white arrowheads). Scale bar: 100µm. Right: Pyramidal cell at higher magnification. Scale bar: 15µm. (**G**) Pyramidal cell plasticity after RWS (N=12 mice) and after pairing with CF activation (RWS+CF; N=11 mice). Right: Quantification of evoked responses across neurons. (**H**) Data in (**G**) binned across time. Blue shading: RWS/RWS+CF. (**I**) Quantification across mice, normalized to the average baseline whisker response. (**J-L**) Analyses for INs in the same mice. Data: mean ± SEM. Scale bars: 0.2 ΔF/F; 0.5s.

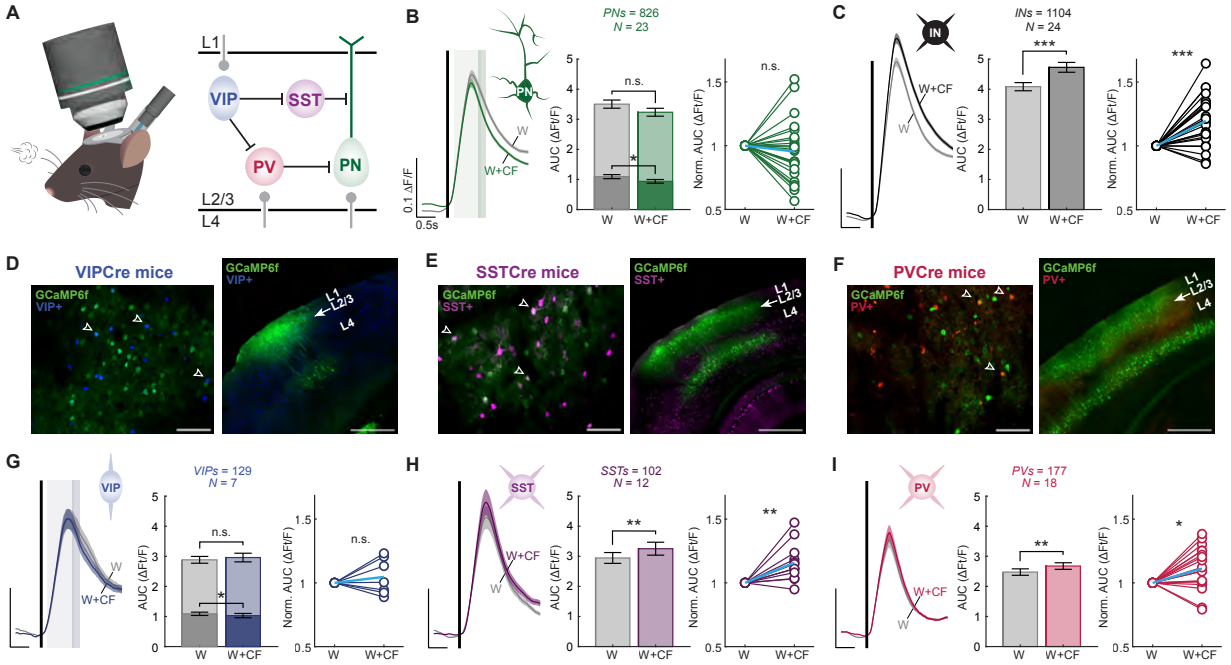

Figure 2. Optogenetic CF co-activation differentially modulates basic responses to whisker stimulation in different types of neocortical neurons. (**A**) Schematic of the recording configuration (left) and S1 cortex microcircuit (right). (**B**) CF co-activation with whisker stimulation does not significantly alter response amplitudes in morphologically identified L2/3 pyramidal neurons (n=826 cells; N=23 mice) in the default analysis window (0-700ms; light shade), but responses decrease in the late response window (650-850ms; dark shade). Left: averaged traces. Middle: analysis by neuron. Shades distinguish analyzed time windows. Right: analysis by mouse (0-700ms). Blue line indicates mean. (**C**) CF co-activation significantly enhances responses in putative interneurons (INs; n=1104 cells; N=24 mice). (**D** – **F**) Sample two-photon field of view (left) and post-hoc verification of expression in S1 using confocal microscopy (right). Arrowheads indicate neurons co-expressing GCaMP6f and tdTomato in VIP interneurons (**D**), SST interneurons (**E**), or PV interneurons (**F**). Scale bars: 100µm (left); 500µm (right). (**G**) CF co-activation with whisker stimulation significantly reduces VIP population responses in the late analysis window (n=129 cells, N=7 mice; shades as in **B**), but enhances responses in SST interneurons (n=102 cells; N=12 mice; **H**) and PV interneurons (n=177 cells; N=18 mice; **I**). Middle plots show analysis by neuron, right plots analysis by mouse (blue line indicates mean). Scale bars: 0.1 ΔF/F; 0.5s. Data: mean ± SEM.

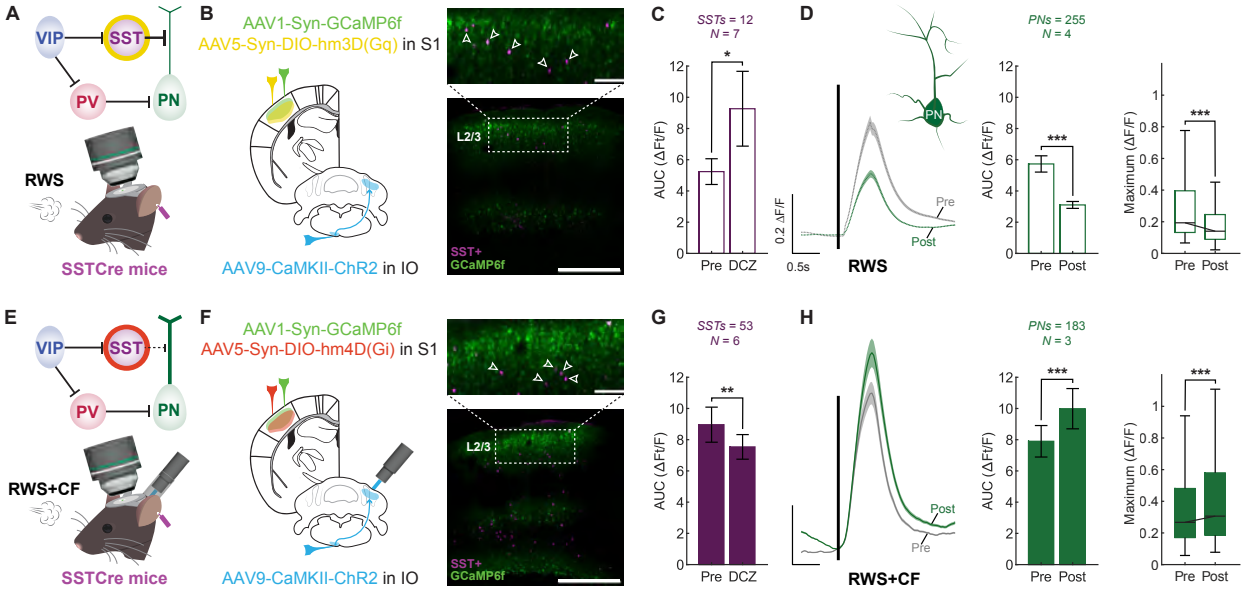

Figure 3. SST interneurons are recruited to prevent L2/3 pyramidal cell plasticity. (**A**) Circuit diagram highlighting the chemogenetic activation of SST interneurons and recording configuration. (**B**) Expression of activating hM3D(Gq) receptors is localized to neocortical SST interneurons. Scale bar: 100µm (top) and 500µm (bottom). (**C**) DCZ application enhances responses in SST interneurons (n=12 cells; N=7 mice). (**D**) In the presence of DCZ, RWS stimulation suppresses L2/3 pyramidal cell potentiation, and even causes depression, even when the CF is not co-activated (n=255 cells; N=4 mice). Left: average traces; middle: analysis by cell (mean ± SEM); right: response range by cell (whiskers: range; box: 25th and 75th percentiles; line: median). (**E**) Circuit diagram highlighting the chemogenetic inhibition of SST interneurons and recording configuration. (**F**) Expression of inhibiting hM4D(Gi) receptors is localized to neocortical SST interneurons. Scale bars as in (**B**). (**G**) DCZ application reduces responses in SST interneurons (n=53 cells; N=6 mice). (**H**) In the presence of DCZ, pyramidal cell potentiation is observed, despite CF-co-activation (n=183 cells; N=3 mice). Data analysis presented as in (**D**). Scale bars: 0.2 ΔF/F; 0.5s.

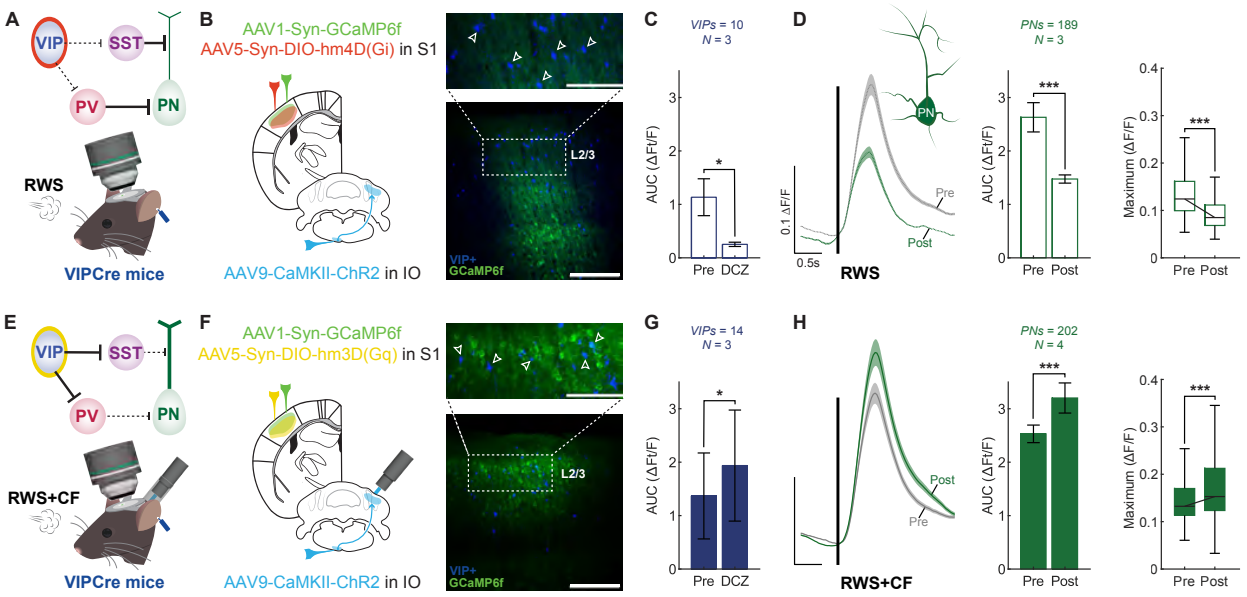

Figure 4. VIP interneurons mediate the effects of optogenetic CF activation. (**A**) Circuit diagram highlighting the chemogenetic inhibition of VIP interneurons and recording configuration. (**B**) Expression of inhibiting hM4D(Gi) receptors is localized to neocortical VIP interneurons. Scale bars: 100µm (top) and 500µm (bottom). (**C**) DCZ application reduces responses in VIP interneurons (n=10 cells; N=3 mice). (**D**) In the presence of DCZ, RWS stimulation suppresses L2/3 pyramidal cell potentiation, and even causes depression, even when the CF is not co-activated (n=189 cells; N=3 mice). Left: averaged traces; middle: analysis by cell (mean ± SEM); right: response range by cell (range; box: 25th and 75th percentiles; line: median). (**E**) Circuit diagram highlighting the chemogenetic activation of VIP interneurons and recording configuration. (**F**) Expression of activating hM3D(Gq) receptors is localized to neocortical VIP interneurons. Scale bars as in (**B**). (**G**) DCZ application enhances responses in VIP interneurons (n=14 cells; N=3 mice). (**H**) In the presence of DCZ, pyramidal cell potentiation is observed, despite CF co-activation (n=202 cells; N=4 mice). Data analysis presented as in (**D**). Scale bars: 0.1 ΔF/F; 0.5s.

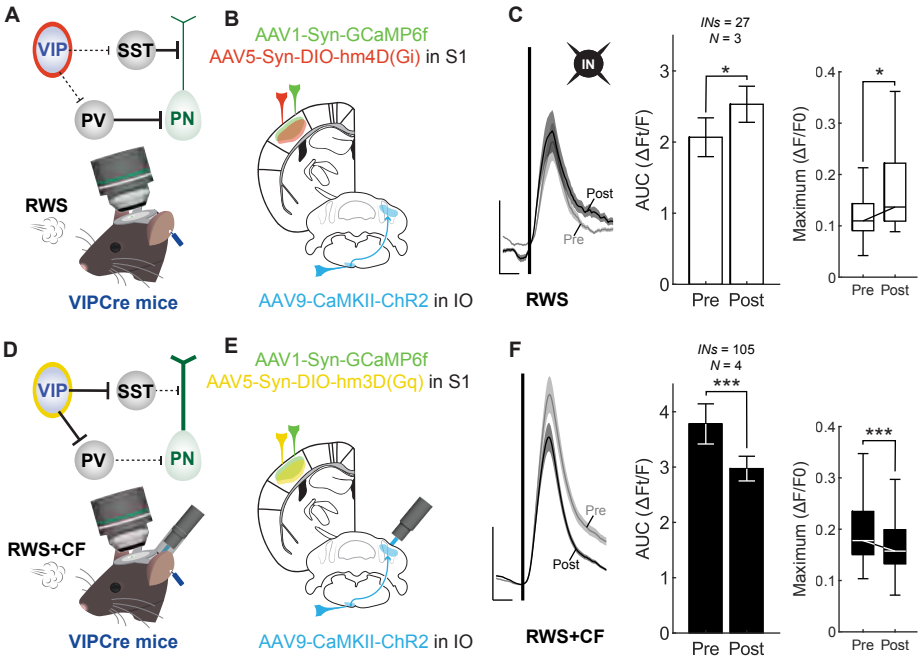

Figure 5. VIP interneurons orchestrate the inhibitory network in S1. (**A**) Circuit diagram highlighting the chemogenetic inhibition of VIP interneurons and recording configuration. (**B**) Inhibiting hM4D(Gi) receptors are expressed in neocortical VIP interneurons. Note A-B are identical to Fig. 4.A-B. (**C**) In the presence of DCZ, RWS stimulation activates L2/3 interneurons, even when the CF is not co-activated (n=27 cells; N=3 mice). Left: averaged traces; middle: analysis by cell (mean ± SEM); right: response range by cell (whiskers: range; box: 25th and 75th percentiles; line: median). (**D**) Circuit diagram highlighting the chemogenetic activation of VIP interneurons and recording configuration. (**E**) Activating hM3D(Gq) receptors are expressed in neocortical VIP interneurons. Note D-E are identical to Fig. 4E-F. (**F**) In the presence of DCZ, IN depression is observed, despite CF co-activation (n=105 cells; N=4 mice). Data analysis presented as in (**C**). Scale bars: 0.2 ΔF/F; 0.5s.

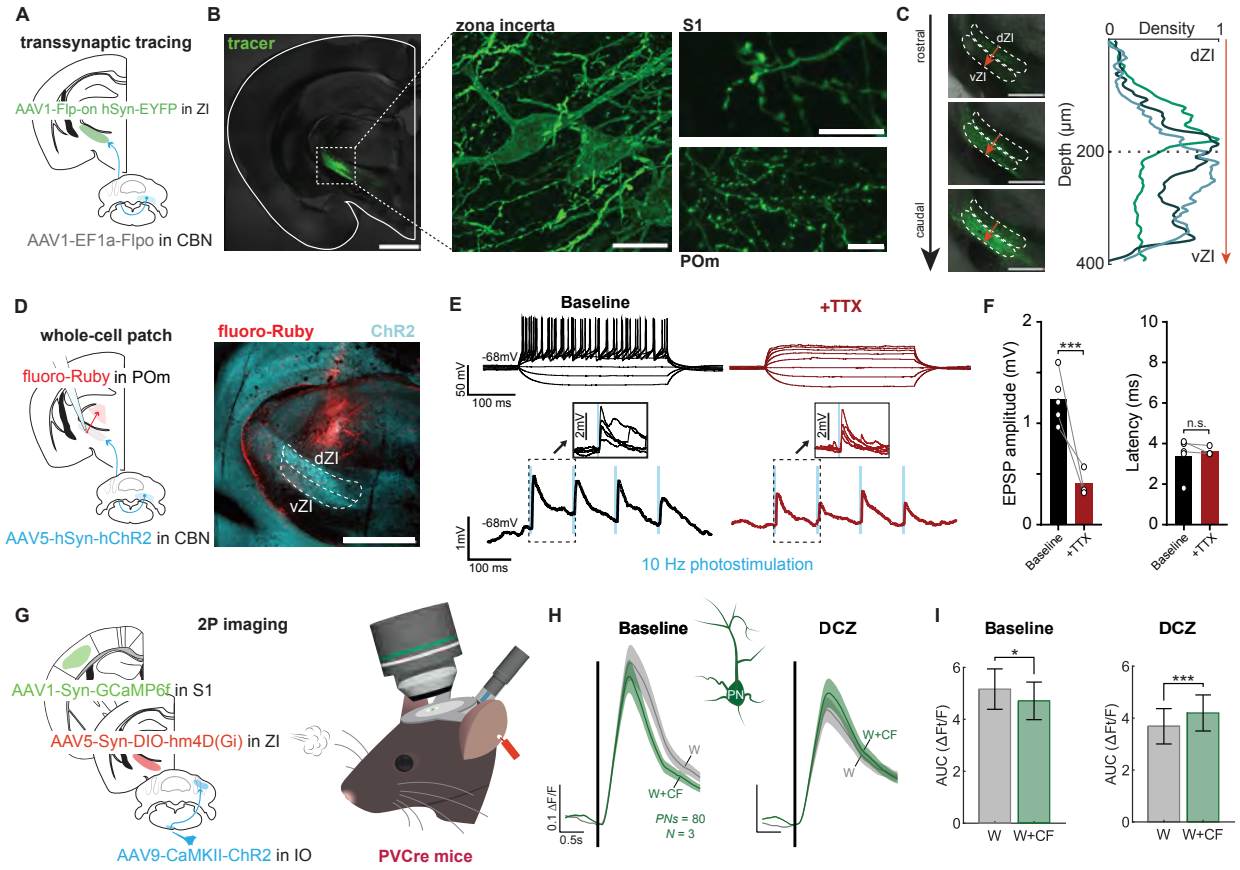

Figure 6. A pathway from the cerebellar nuclei via the zona incerta and thalamic nucleus POm to S1 cortex. (**A**) Schematic of dual-injection strategy to label outputs of zona incerta (ZI) neurons receiving input from contralateral cerebellar nuclei. Scale bar: 1mm. (**B**) EYFP expression in ZI (left) with a higher-magnification image (same slice). Right: labeled axons in the posterior medial nucleus (POm; bottom; scale bar: 20µm) and S1 cortex (top; scale bar: 10µm). (**C**) Distribution of projections from cerebellar nuclei to the ZI along the rostro-caudal axis; dotted line separates ventral (vZI) and dorsal ZI (dZI). Scale bars: 500µm. (**D**) Labeling strategy for recordings shown in (**E**). Scale bar: 1mm. (**E**) Top: Whole-cell patch-clamp recordings from POm-projecting ZI neurons receiving innervation from cerebellar nuclei. Responses to depolarizing current pulses in the absence (left) and presence (right) of TTX (1µM). Bottom: Responses to photostimulation of ChR2-expressing terminals from cerebellar nuclei neurons. (**F**) Amplitude (left) of photostimulation-evoked EPSPs and latency (right) in control recordings (n=5) and after wash-in of TTX (n=3). (**G**) Experimental configuration for recordings from mice expressing inhibiting hM4D(Gi) receptors in PV-expressing ZI interneurons. (**H**) In the presence of DCZ, the suppressive effect of CF co-activation on basic whisker responses in L2/3 pyramidal neurons is blocked (n=80 cells; N=3 mice). (**I**) Bar graphs: analysis by neuron. Data: mean ± SEM. Scale bars: 0.1 ΔF/F; 0.5s.

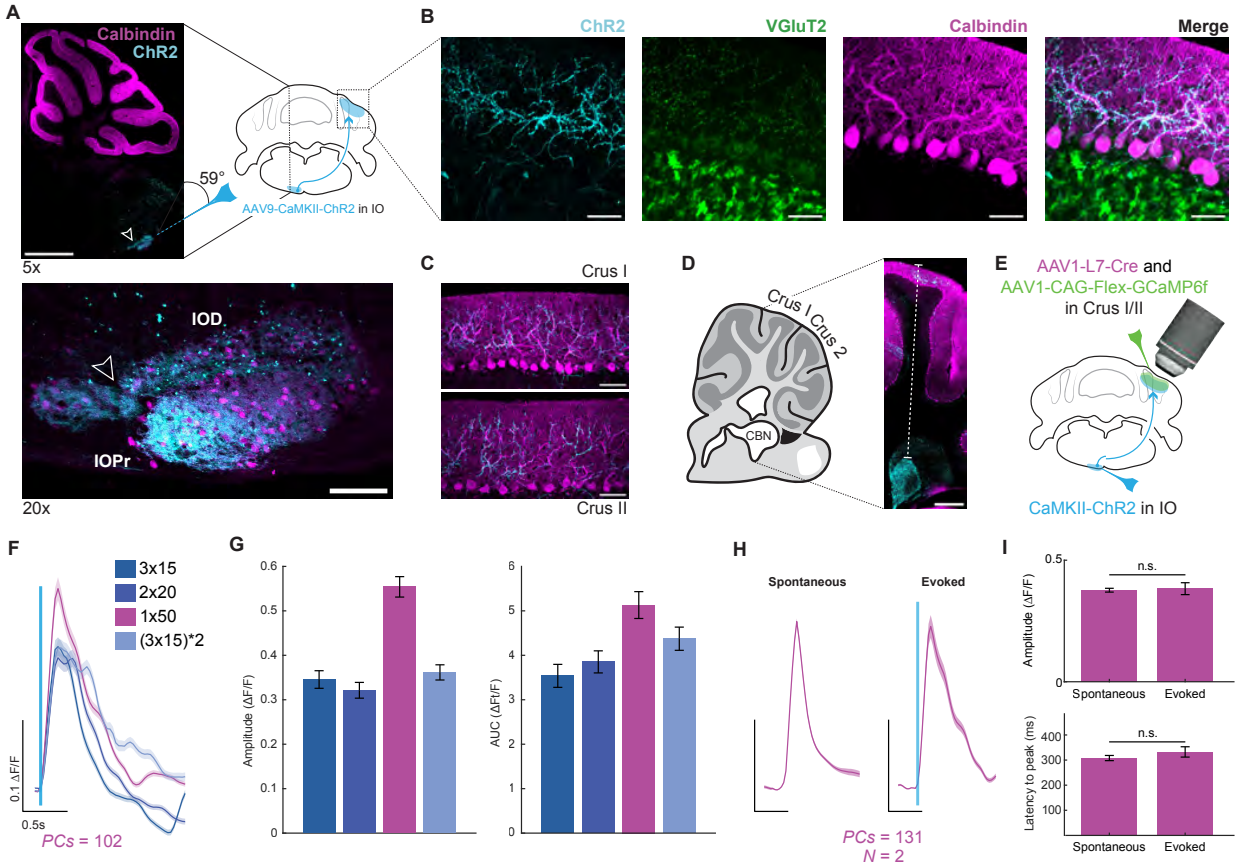

Supplementary Figure 1. Optogenetic CF activation causes GCaMP6f-encoded calcium transients in Purkinje cells. (**A**) Schematic of IO injection. Top left: Cerebellum (calbindin-staining of PCs) and IO (as in Fig 1B). Bottom: ChR2 expression in the IO principal (IOPr) and dorsal IO (IOD). Scale bars: 1mm (top) and 100µm (bottom). (**B**) Overlap of VGluT2-stained CF terminals with ChR2 expression in the contralateral cerebellar cortex. Scale bar: 40µm. (**C**) Post-hoc verification of ChR2 expression in CF terminals in crus I and II. Scale bars: 50µm. (**D**) Measure of distance of the pial surface to the cerebellar nuclei. While the IO innervates both the cerebellar cortex and nuclei directly, it is unlikely that CF terminals other than the superficial ones innervating PCs are optogenetically activated as the intensity of blue light decreases exponentially in brain tissue. Scale bar: 300µm. Dashed line: 2mm. (**E**) Experimental schematic for F-I. (**F**) Test of various stimulus protocols: 3x15ms, 2x20ms, 1x50ms (interval 50ms) and (3x15ms)*2 (interval 50ms). Traces show response averages (n=102 cells from one mouse). (**G**) Bar graphs showing response peaks (left) and integrals (right) from the corresponding data in f. Data: mean ± SEM. (**H**) Calcium transients evoked by 470nm, 50ms LED light pulses in PCs in crus I/II (n=131 cells; N=2 mice) in comparison to spontaneous events (left). Scale bars: 0.1 ΔF/F; 0.5s. (**I**) Amplitude and latency to peak measures from the corresponding data in h. Data: mean ± SEM. Scale bars: 0.1 ΔF/F; 0.5s.

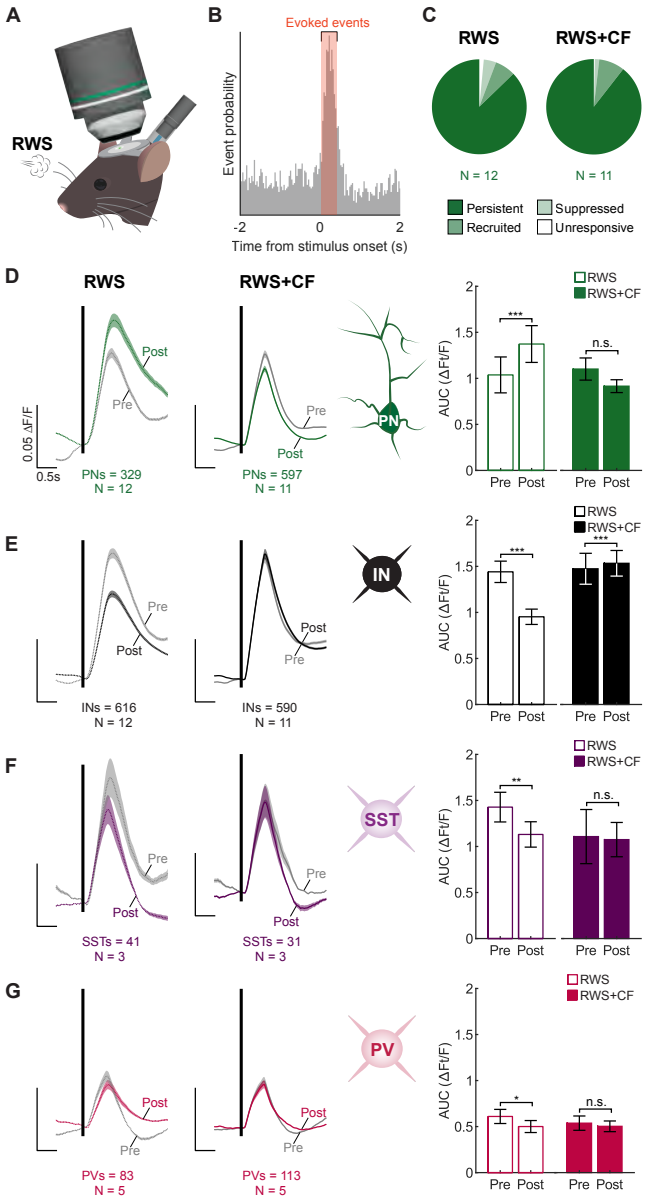

Supplementary Figure 2. Plasticity in different neuron types. (**A**) Experimental schematic. (**B**) Event probability around stimulus onset with the window for detection of stimulus-evoked events (red; three standard deviations above the mean event probability, calculated across all frames collected during the 20-second trial periods). (**C**) Pie chart indicating the percentage of L2/3 pyramidal cells recruited or suppressed by RWS/RWS+CF activity (only responsive to whisker stimulation in post- or pre- periods, respectively) and how many remained entirely unresponsive. (**D**) Left: RWS-evoked response changes in L2/3 pyramidal neurons (n=329 cells; N=12 mice). Right: RWS+CF-evoked response changes in L2/3 pyramidal neurons (n=597 cells; N=11 mice). Bar graphs quantify calcium responses across all cells and trials (i.e. including unresponsive neurons and trials without whisker-evoked responses). (**E**) The same as D in INs in the same mice (n=616 cells for RWS; n=590 cells for RWS+CF). (**F, G**) Same as (D, E) in tdTomato-tagged SST interneurons (F; n=41 cells and N=3 mice for RWS; n=31 cells and N=3 mice for RWS+CF) and PV interneurons (G; n=83 cells; N=5 mice for RWS; n=113 cells; N=5 mice for RWS+CF). Scale bars: 0.05 ΔF/F; 0.5s. Data: mean ± SEM.

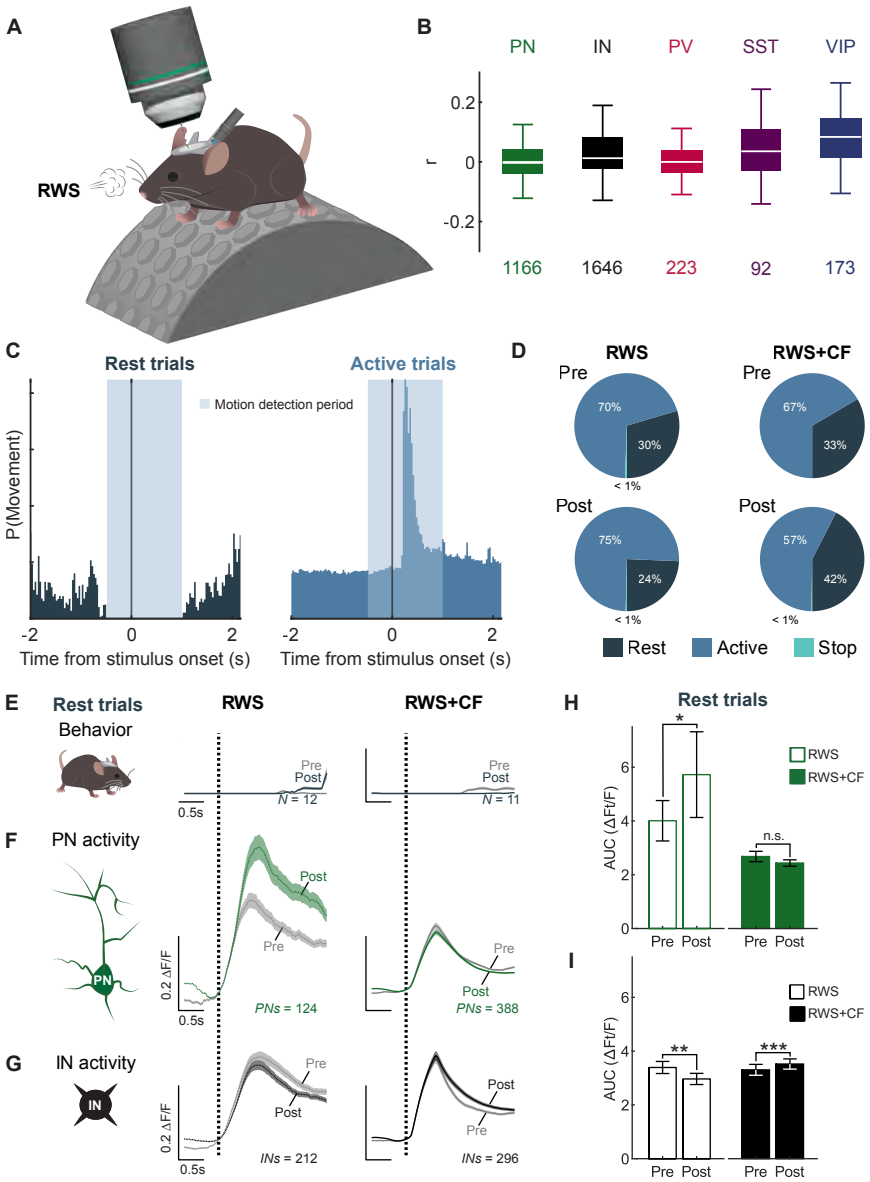

Supplementary Figure 3. Impact of RWS- and RWS+CF-stimulation on animal motion. (**A**) Experimental schematic. Mice are awake and head-fixed but can walk/run on the treadmill. (**B**) Average cross-correlation coefficient between neural calcium signals and movement activity data, segregated by neuron type. The numbers below the box charts indicate the number of recorded cells. (**C**) Left: probability distribution of animal movement in Rest trials, demonstrating the absence of movement both before and after stimulus onset. Right: probability distribution of animal movement in Active trials. (**D**) Pie charts indicating the percentage of rest, active and stop trials pre-vs post-RWS (left) or RWS+CF (right). (**E**) Average probability of animal movement in Rest trials pre- and post-RWS (left) or RWS+CF (right) over the same time scale as the neural traces shown below. (**F**) and (**H**) RWS-evoked potentiation in L2/3 pyramidal neurons (n=124; N=12) and RWS+CF-mediated suppression of potentiation (n=388; N=11) in the absence of animal movement (i.e. in Rest trials). (**G**) and (**I**) Analysis for INs in the same mice (n=212 cells for RWS; n=296 cells for RWS+CF). Scale bars: 0.1 ΔF/F; 0.5s. Data: mean ± SEM. Note motion activity traces capture both whisking and running activity. Scale bars: 0.1 ΔF/F; 0.5s.

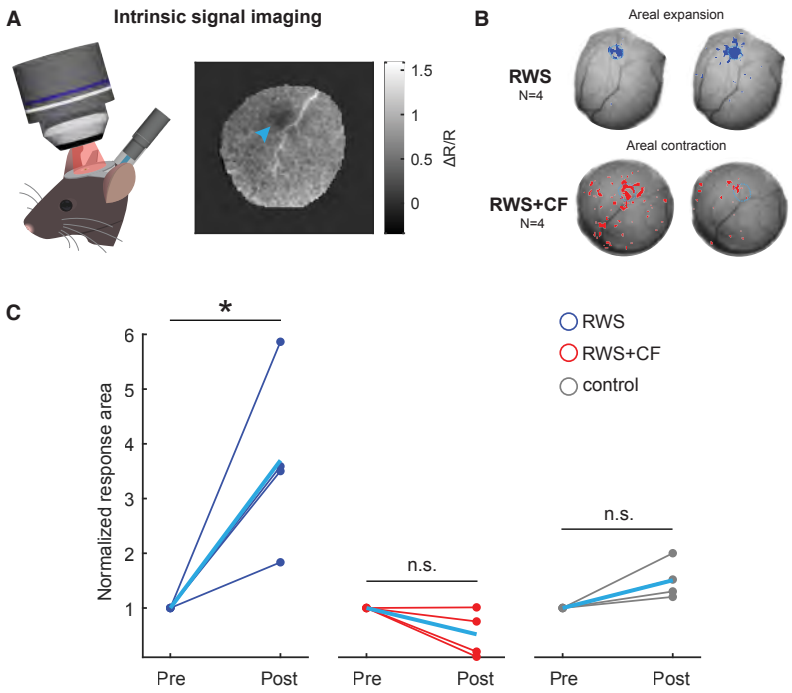

Supplementary Figure 4. Intrinsic optical imaging confirms CF-mediated suppression of S1 plasticity. (**A**) Experimental schematic. Intrinsic optical imaging is performed using a high-speed camera. The field of view is illuminated with red light (625 nm). A decrease in reflectance indicates increased oxygen consumption by neurons activated by single whisker stimulation (blue arrow). (**B**) Top: Example of S1 plasticity evoked by stimulation of the C2 whisker at 10Hz. Bottom: Example of suppression of response potentiation when whisker stimulation is paired with optogenetic CF co-activation at 1Hz. (**C**) Quantification of RWS-evoked potentiation of the single whisker response area (blue; N=4 mice) and RWS+CF-mediated suppression of response potentiation (red; N=4 mice). No response potentiation is observed in the absence of repeated whisker stimulation or CF activation (grey; N=4 mice). Data are normalized to the baseline response area. Light blue line indicates mean.

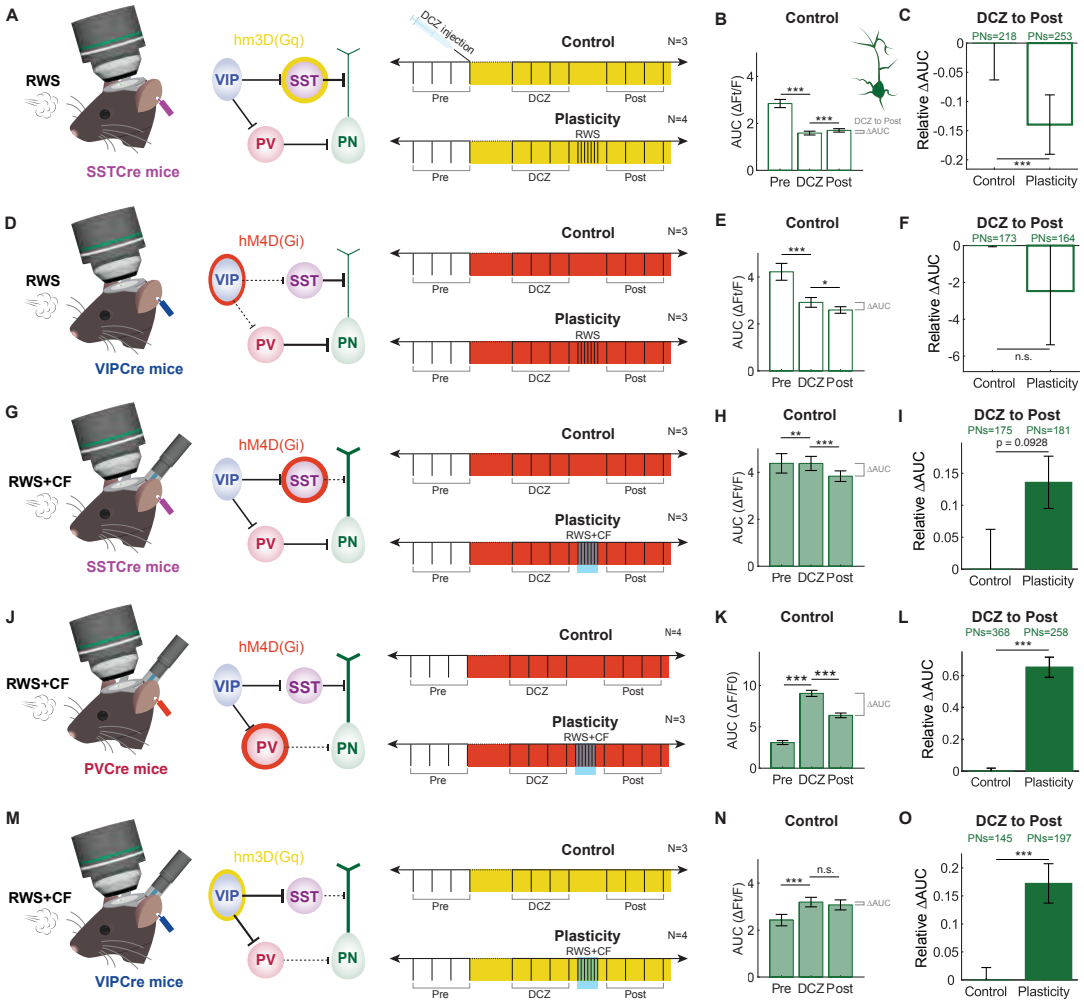

Supplementary Figure 5. Chemogenetic manipulation of interneuron activity: plasticity effects in L2/3 pyramidal cells vs control. (**A**) Chemogenetic activation of SST interneurons. Left: Experimental schematic. Middle: circuit diagram. Right: DCZ injection activates SST interneurons (yellow). Top: Control protocol. 'Post' marks the period equivalent in time to the period for the measurement of plasticity effects after RWS (bottom). (**B**) Response amplitudes in L2/3 pyramidal neurons during Pre, DCZ wash-in, and Post periods in control experiments. (**C**) The difference in response (ΔAUC) of L2/3 pyramidal cells to whisker stimulation between the DCZ wash-in and Post periods; (control: n=218 cells; N=3 mice; plasticity: n=253 cells; N=4 mice); negative ΔAUC values indicate AUC values in the Post period are lower than in the DCZ wash-in period. The ΔAUC in control and plasticity experiments are normalized to the absolute ΔAUC in control experiments to demonstrate changes in the plasticity experiments relative to controls. Note the absence of PN potentiation in the plasticity experiment. (**D**) – (**F**) Equivalent measures during chemogenetic VIP interneuron inhibition (red; control: n=173 cells; N=3 mice; plasticity: n=164 cells; N=3 mice). Note the absence of PN potentiation in the plasticity experiment. (**G**) – (**I**) Equivalent measures during chemogenetic SST interneuron inhibition (control: n=175 cells; N= 3 mice; plasticity: n=181 cells; N=3 mice). (**J**) – (**L**) Equivalent measures during chemogenetic PV interneuron inhibition (control: n=368 cells; N=4 mice; plasticity: n=258 cells; N=3 mice). PN neurons are significantly potentiated after plasticity experiments beyond changes in controls. (**m**) – (**o**) Equivalent measures during chemogenetic VIP interneuron activation (control: 145 cells; N=3 mice; plasticity: n=197 cells; N=4 mice). PN neurons are significantly potentiated after plasticity experiments beyond changes in controls. Optogenetic CF co-activation is applied during RWS in the experiments shown in (**G**) – (**O**). Data: mean ± SEM.

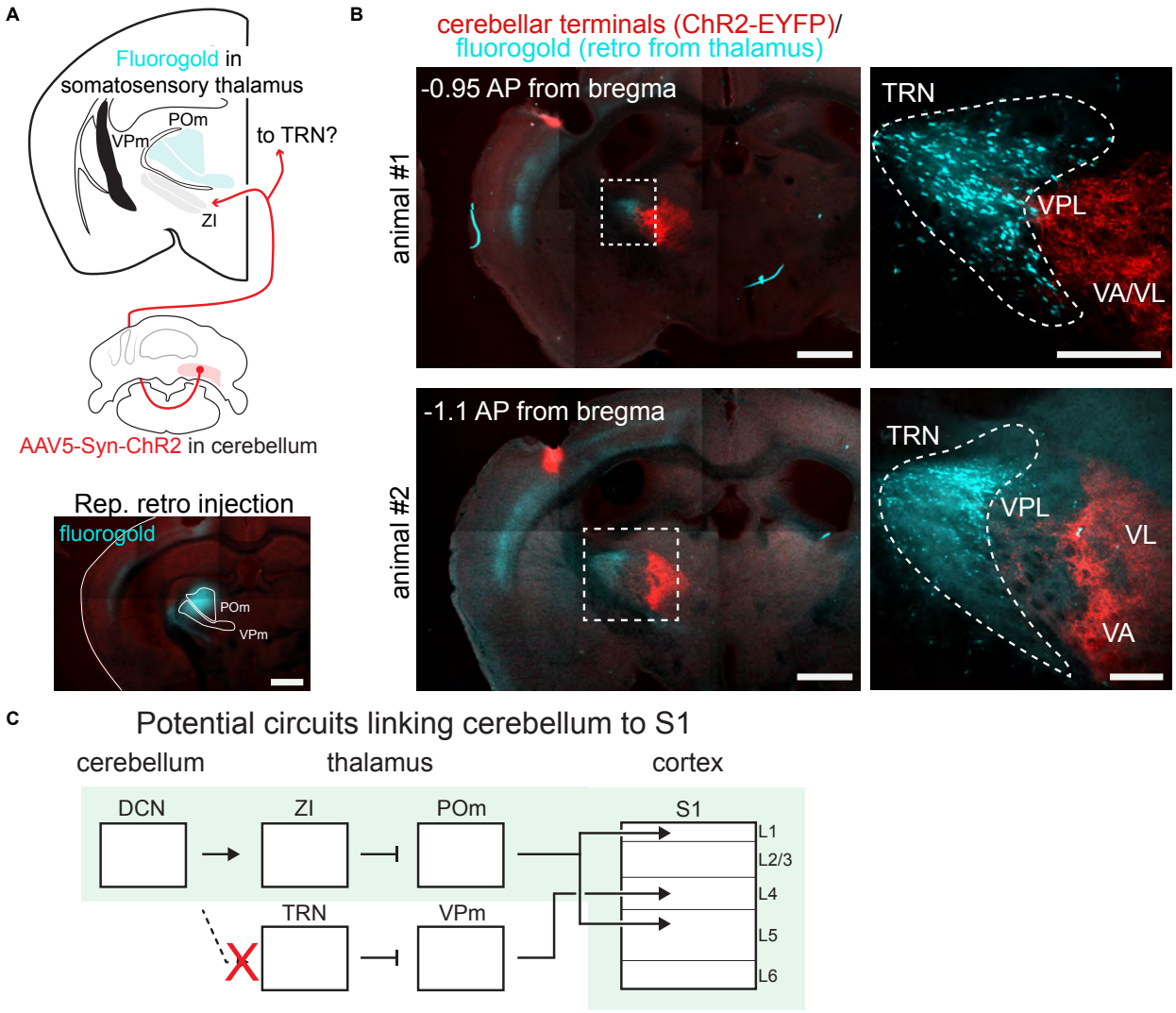

Supplementary Figure 6. Cerebellar nuclei do not strongly project to thalamic reticular nucleus. (**A**) Schematic of labeling approach (top) and injection site of retrograde tracer (bottom). Scale bar: 1mm. (**B**) Image of retrograde label from the somatosensory thalamus (POm and VPM; cyan) and orthograde label from the contralateral cerebellar nuclei (red) taken approximately -1.0mm posterior from bregma, demonstrating lack of overlap between neurons in the thalamic reticular nucleus (TRN) and cerebellar nuclei terminals in the adjacent thalamic nuclei. Representative images are shown from two separate mice. Scale bars: 1mm (left images) and 250µm (right images). (**C**) Projection diagram. DCN: deep cerebellar nuclei; ZI: zona incerta; POm: posterior medial thalamic nucleus; TRN: thalamic reticular nucleus; VPM: ventral posterior medial nucleus; VPL: ventral posterior lateral nucleus; VA: ventral anterior nucleus; VL: ventral lateral nucleus.

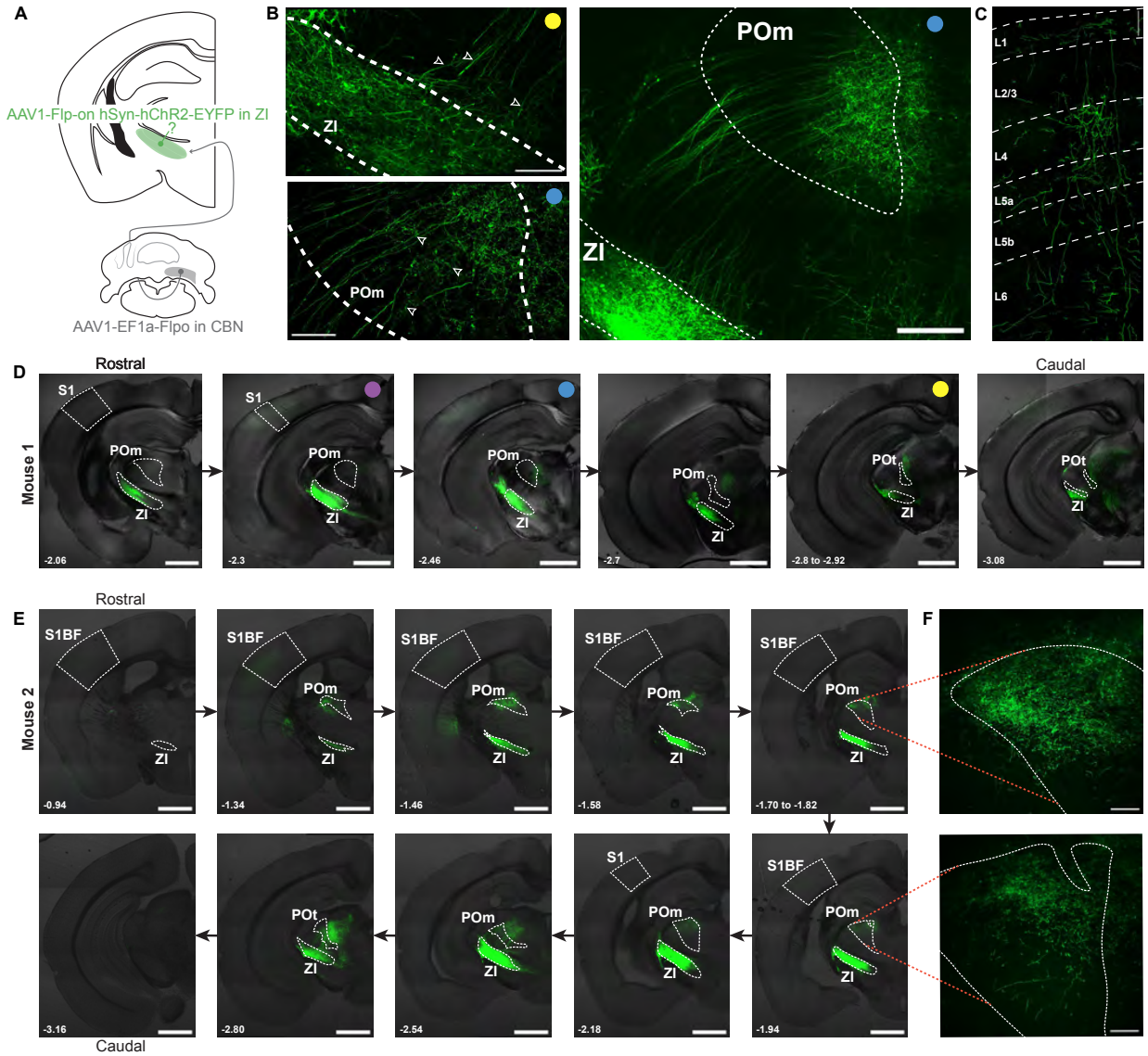

Supplementary Figure 7. Transsynaptic labeling identifies projections from the cerebellar nuclei to POm. (**A**) Schematic of dual-injection approach to label outputs of ZI neurons receiving input from the contralateral CBN. (**B**) Top left: EYFP-expressing terminals and cell bodies within ZI (dashed lines) and axonal projections out of the ZI (arrowheads). Scale bar: 100µm. Bottom left: projections from the ZI terminate in POm (arrowheads). Scale bar: 50 µm. Right: zoomed-out view showing projections from ZI to POm in the same plane. Scale bar: 200 µm. (**C**) ZI neurons receiving cerebellar input project to S1. Synaptic terminals are observed in L1 and L5a. Scale bar: 100 µm. (**D**) Series of coronal sections showing details of the projections from the contralateral CBN to ZI and POm. Scale bars: 1mm. (**E**) The same as D in a second mouse, showing robust EYFP expression across the rostro-caudal extent of ZI. Scale bars: 1mm. POt = posterior thalamic nucleus (triangular part). Colored dots mark images taken from the same sections.

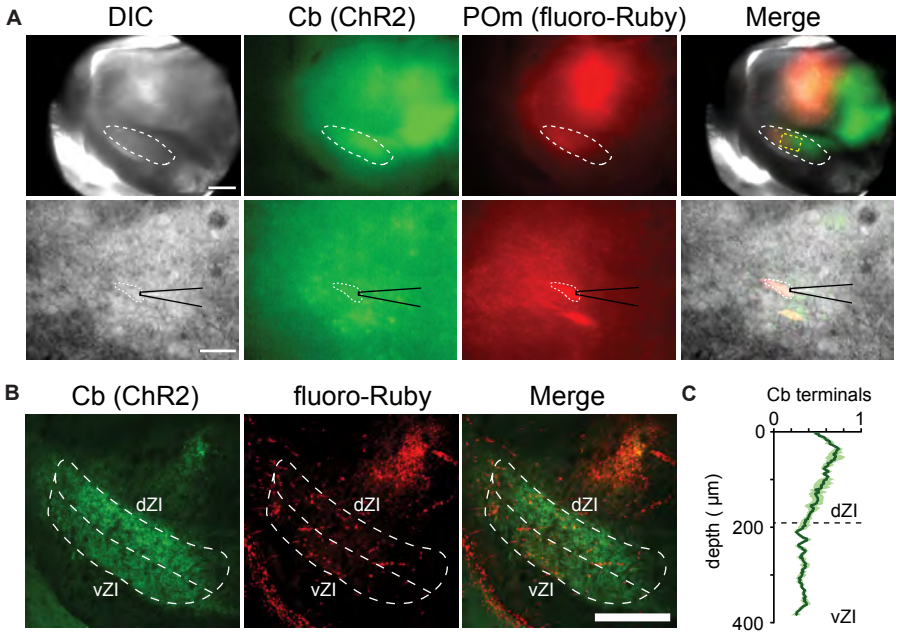

Supplementary Figure 8. Whole-cell patch-clamp recordings are performed from neurons in the ZI that project to POm and receive input from cerebellar nuclei. (**A**) Left: Differential interference contrast (DIC) image showing the ZI (white dashed circle) at low magnification (top; scale bar: 500µm), and a neuron selected for patching at higher magnification (bottom; scale bar: 100µm). Middle left: same images showing ChR2-expression. Middle right: same images showing retrograde fluoro-Ruby label originating in the POm. Right: merged images (boxed area with yellow dashed line marks the recordings area shown in the images below). (**B**) Post-hoc histology of an acute slice used for recordings demonstrating the details of cerebellar innervation of the ZI, separated by dorsal ZI (dZI) and ventral ZI (vZI; image corresponds to Fig. 5D, separated by channel). Scale bar: 500µm. (**C**) Quantification of the terminal fluorescence segregated by dZI and vZI. Data: mean ± SEM.

panel		mean	median	error	n cells	N mice	test	*P* value	result	measurement (units)	cell type
1.C		0.554	0.5004	0.023	102	1	N/A	N/A	N/A	Amplitude (ΔF/F)	PC
1.G	Pre (RWS)	3.9581	2.3941	0.3824	287†	12	Wilcoxon	0.0010	**	AUC ((ΔF*t)/F)	PN
	Post (RWS)	5.246	2.4812	0.6725							
	Pre (RWS+CF)	3.2676	1.9988	0.1811	534†	11	Wilcoxon	0.1126	n.s.		
	Post (RWS+CF)	2.6892	2.0035	0.1049							
1.H	-40 min (RWS)	4.65488	N/A	0.5261	144†	10	Two-way ANOVA (Group comparison)	<0.001	***	AUC ((ΔF*t)/F)	PN
	-30 min (RWS)	3.91113		0.4083	174†	11					
	-20 min (RWS)	3.65761		0.3639	172†	11					
	-10 min (RWS)	3.91723		0.4911	213†	12					
	0 min (RWS)‡	4.19536		0.7388	100†	7					
	10 min (RWS)‡	5.77819		0.8127	212†	12					
	20 min (RWS)‡	6.48013		1.7059	217†	12					
	30 min (RWS)‡	5.91206		0.7591	155†	10					
	40 min (RWS)‡	5.64781		0.8828	157†	10					
	50 min (RWS)‡	5.16045		0.6085	117†	9					
	60 min (RWS)‡	5.02273		0.7503	54†	4					
	- 40 min (RWS+CF)	3.32904		0.2981	351†	10					
	-30 min (RWS+CF)	3.60127		0.3131	317†	10					
	- 20 min (RWS+CF)	3.69046		0.2739	364†	10					
	-10 min (RWS+CF)	3.05876		0.2269	394†	11					
	0 min (RWS+CF)‡	3.87257		0.423	204†	9					
	10 min (RWS+CF)‡	2.37707		0.1063	479†	11					
	20 min (RWS+CF)‡	2.61932		0.1256	511†	11					
	30 min (RWS+CF)‡	2.74055		0.1435	483†	10					
	40 min (RWS+CF)‡	2.32432		0.1067	477†	10					
	50 min (RWS+CF)‡	2.49962		0.1297	362†	6					
	60 min (RWS+CF)‡	2.80165		0.233	352†	4					
1.I	Pre (RWS)	1	N/A	0	287	12†	One-sample t-test	0.0104	*	AUC ((ΔF*t)/F)	PN
	Post (RWS)	1.2629		0.0853							
	Pre (RWS+CF)	1		0	534	11†	One-sample t-test	0.003	**		
	Post (RWS+CF)	0.7723		0.0584							
1.J	Pre (RWS)	3.8936	2.7519	0.1701	570†	12	Wilcoxon	<0.001	***	AUC ((ΔF*t)/F)	IN
	Post (RWS)	3.0852	2.2592	0.1194							
	Pre (RWS+CF)	3.5683	2.3499	0.2021	516†	11	Wilcoxon	<0.001	***		
	Post (RWS+CF)	3.8983	2.5878	0.1797							
1.K	-40 min (RWS)	4.70089	N/A	0.286	342†	10	Two-way ANOVA (Group comparison)	0.0127	*	AUC ((ΔF*t)/F)	IN
	-30 min (RWS)	3.69953		0.2221	380†	11					
	-20 min (RWS)	4.15268		0.266	324†	11					
	-10 min (RWS)	3.83042		0.21	446†	12					
	0 min (RWS)‡	4.50767		0.3892	207†	7					
	10 min (RWS)‡	3.47265		0.1809	438†	12					
	20 min (RWS)‡	3.31423		0.1744	434†	12					
	30 min (RWS)‡	3.47938		0.1832	311†	10					
	40 min (RWS)‡	3.66121		0.1901	335†	9					
	50 min (RWS)‡	3.24975		0.2246	239†	9					
	60 min (RWS)‡	3.16086		0.2327	147†	4					
	- 40 min (RWS+CF)	3.93255		0.3137	320†	10					
	-30 min (RWS+CF)	4.4692		0.396	283†	11					
	- 20 min (RWS+CF)	5.02758		0.3417	344†	10					
	-10 min (RWS+CF)	3.95778		0.278	376†	11					
	0 min (RWS+CF)‡	4.11703		0.4043	219†	10					
	10 min (RWS+CF)‡	3.7648		0.2121	444†	11					
	20 min (RWS+CF)‡	3.87636		0.2234	479†	11					
	30 min (RWS+CF)‡	3.90208		0.2237	423†	10					
	40 min (RWS+CF)‡	3.37561		0.1953	405†	10					
	50 min (RWS+CF)‡	3.8697		0.2619	314†	6					
	60 min (RWS+CF)‡	4.25666		0.2688	273†	4					
1.L	Pre (RWS)	1	N/A	0	570	12†	One-sample t-test	<0.001	***	AUC ((ΔF*t)/F)	IN
	Post (RWS)	0.7983		0.0252							
	Pre (RWS+CF)	1		0	516	11†	One-sample t-test	0.2233	n.s.		
	Post (RWS+CF)	1.1321		0.1018							

† indicates whether statistics performed across cells or mice
‡ time points included in ANOVA

Data S1.
Data and statistical tests corresponding to Figure 1.

panel		mean	median	error	n cells	N mice	test	*P* value	result	measurement (units)	cell type
2.B (c)	W (0-700ms)	3.5038	2.3648	0.1358	826†	23	Wilcoxon	0.1856	n.s.	AUC ((ΔF*t)/F)	PN
	W+CF (0-700ms)	3.2344	2.2292	0.1314							
	W (650-850ms)	1.0935	0.4922	0.0672			Wilcoxon	0.0487	*		
	W+CF (650-850ms)	0.937	0.4763	0.0611							
2.C (r)	W	1	N/A	0	826	23†	One-sample t-test	0.3709	n.s.	AUC ((ΔF*t)/F)	PN
	W+CF	0.954		0.0504							
2.C (c)	W	4.0841	2.8209	0.1357	1104†	24	Wilcoxon	<0.001	***	AUC ((ΔF*t)/F)	IN
	W+CF	4.7268	3.1189	0.1637							
2.C (r)	W	1	N/A	0	1104	24†	One-sample t-test	<0.001	***	AUC ((ΔF*t)/F)	IN
	W+CF	1.1961		0.0406							
2.G (c)	W (0-700ms)	2.883	2.529	0.1128	129†	7	Wilcoxon	0.8665	n.s.	AUC ((ΔF*t)/F)	VIP
	W+CF (0-700ms)	2.9589	2.5207	0.1438							
	W (650-850ms)	1.0888	0.9519	0.0545			Wilcoxon	0.0255	*		
	W+CF (650-850ms)	1.0294	0.8138	0.0713							
2.G (r)	W	1	N/A	0	129	7†	One-sample t-test	0.4113	n.s.	AUC ((ΔF*t)/F)	VIP
	W+CF	1.047		0.0533							
2.H (c)	W	2.9453	2.3916	0.18	102†	12	Wilcoxon	0.001	**	AUC ((ΔF*t)/F)	SST
	W+CF	3.2532	2.7647	0.2152							
2.H (r)	W	1	N/A	0	102	12†	One-sample t-test	0.0035	**	AUC ((ΔF*t)/F)	SST
	W+CF	1.1582		0.0427							
2.I (c)	W	2.4758	2.269	0.107	177†	18	Wilcoxon	0.0032	**	AUC ((ΔF*t)/F)	PV
	W+CF	2.6768	2.369	0.1092							
2.I (r)	W	1	N/A	0	177	18†	One-sample t-test	0.0127	*	AUC ((ΔF*t)/F)	PV
	W+CF	1.1122		0.0403							

† indicates whether statistics performed across cells or mice

Data S2.
Data and statistical tests corresponding to Figure 2.

panel		mean	median	error	n cells	N mice	test	*P* value	result	measurement (units)	cell type
3.C	Pre	5.2386	4.0088	0.8243	12	7	Wilcoxon	0.0425	*	AUC ((ΔF*t)/F)	SST
	DCZ	9.2671	5.9757	2.3962							
3.D (c)	Pre	5.7312	2.927	0.5212	255	4	Wilcoxon	<0.001	***	AUC ((ΔF*t)/F)	PN
	Post	3.106	1.9677	0.2207							
3.D (r)	Pre	0.3938	0.1934	0.0358	255	4	Wilcoxon	<0.001	***	Amplitude (ΔF/F)	PN
	Post	0.2139	0.1403	0.015							
3.G	Pre	8.9616	7.5298	1.1235	53	6	Wilcoxon	0.0057	**	AUC ((ΔF*t)/F)	SST
	DCZ	7.5387	6.4485	0.7883							
3.H (c)	Pre	7.8992	4.0365	1.0087	183	3	Wilcoxon	<0.001	***	AUC ((ΔF*t)/F)	PN
	Post	9.9871	4.5967	1.2894							
3.H (r)	Pre	0.5334	0.267	0.0682	183	3	Wilcoxon	<0.001	***	Amplitude (ΔF/F)	PN
	Post	0.6759	0.3062	0.0872							
4.C	Pre	1.1339	0.8779	0.3452	10	3	Paired t-test	0.0272	*	AUC ((ΔF*t)/F)	VIP
	DCZ	0.2521	0.2239	0.04							
4.D (c)	Pre	2.6299	1.8696	0.2739	189	3	Wilcoxon	<0.001	***	AUC ((ΔF*t)/F)	PN
	Post	1.4749	1.2773	0.0768							
4.D (r)	Pre	0.179	0.1242	0.02	189	3	Wilcoxon	<0.001	***	Amplitude (ΔF/F)	PN
	Post	0.1021	0.0849	0.0055							
4.G	Pre	1.3677	0.2754	0.8043	14	3	Wilcoxon	0.0494	*	AUC ((ΔF*t)/F)	VIP
	DCZ	1.9361	0.4533	1.0391							
4.H (c)	Pre	2.53	1.9726	0.1644	202	4	Wilcoxon	<0.001	***	AUC ((ΔF*t)/F)	PN
	Post	3.2011	2.2506	0.2818							
4.H (r)	Pre	0.1813	0.1324	0.0142	202	4	Wilcoxon	<0.001	***	Amplitude (ΔF/F)	PN
	Post	0.2309	0.1529	0.0226							
5.C (c)	Pre	2.0677	1.4505	0.2728	27	3	Wilcoxon	0.0174	*	AUC ((ΔF*t)/F)	IN
	Post	2.5314	2.1002	0.2536							
5.C (r)	Pre	0.1400	0.1096	0.0181	27	3	Wilcoxon	0.0198	*	Amplitude (ΔF/F)	IN
	Post	0.1740	0.1366	0.0181							
5.F (c)	Pre	3.7801	2.5438	0.3629	105	4	Wilcoxon	<0.001	***	AUC ((ΔF*t)/F)	IN
	Post	2.9725	2.2871	0.2231							
5.F (r)	Pre	0.2656	0.1778	0.0263	105	4	Wilcoxon	<0.001	***	Amplitude (ΔF/F)	IN
	Post	0.2052	0.1572	0.0162							

Data S3.

Data and statistical tests corresponding to Figures 3, 4, and 5.

panel		mean	median	error	n cells	N mice	test	*P* value	result	measurement (units)	cell type
6.F	baseline	1.2386	N/A	0.11	5	5	Welch's t-test	<0.001	***	EPSP amplitude (mV)	ZI neuron
	+TTX	0.4094		0.081	3	3					
	baseline	3.4		0.4159	5	5	Welch's t-test	0.62	n.s.	Latency (ms)	
	+TTX	3.633		0.1333	3	3					
6.I	W (Baseline)	5.1648	3.2461	0.778	80	3	Wilcoxon	0.0183	*	AUC ((ΔF*t)/F)	PN
	W+CF (Baseline)	4.7113	3.1395	0.7239							
	W (DCZ)	3.6838	2.5494	0.6804			Wilcoxon	<0.001	***		
	W+CF (DCZ)	4.1972	2.7795	0.6946							

Data S4.
Data and statistical tests corresponding to Figure 5.

panel		mean	median	error	n cells	N mice	test	*P* value	Result	measurement (units)	cell type
S1.G (l)	3x15	0.3455	N/A	0.0198	102	1	N/A	N/A	N/A	Amplitude (ΔF/F)	PC
	2x20	0.3213		0.0177							
	1x50	0.554		0.023							
	(3x15)*2	0.3616		0.0171							
S1.G (r)	3x15	3.5376	N/A	0.2585	102	1	N/A	N/A	N/A	AUC ((ΔF*t)/F)	PC
	2x20	3.8521		0.2483							
	1x50	5.1302		0.3019							
	(3x15)*2	4.3732		0.261							
S1.I (t)	Spontaneous	0.3768	0.3777	0.0078	131	2	Paired t-test	0.785	n.s.	Amplitude (ΔF/F)	PC
	Evoked	0.3831	0.3184	0.0245							
S1.I (b)	Spontaneous	308.355	290.51	10.308	131	2	Wilcoxon	0.0875	n.s.	Latency to peak (ms)	PC
	Evoked	332.761	258.231	20.567							

Data S5.

Data and statistical tests corresponding to Supplementary Figure 1.

panel		mean	median	error	%	n cells	N mice	test	*P* value	result	measurement (units)	cell type
S2.C	Persistent (RWS)	N/A	N/A	N/A	87.23	329†	12	Chi-squared	0.0103	*	percent total cells (%)	PN
	Recruited (RWS)				6.991							
	Suppressed (RWS)				4.255							
	Unresponsive (RWS)				1.52							
	Persistent (RWS+CF)				89.45	597†	11					
	Recruited (RWS+CF)				8.71							
	Suppressed (RWS+CF)				1.508							
	Unresponsive (RWS+CF)				0.335							
S2.D	Pre (RWS)	1.0374	0.4502	0.1950	N/A	329†	12	Wilcoxon	<0.001	***	AUC ((ΔF*t)/F	PN
	Post (RWS)	1.3728	0.5007	0.1998								
	Pre (RWS+CF)	1.1012	0.4755	0.1203		597†	11	Wilcoxon	0.9575	n.s.		
	Post (RWS+CF)	0.9152	0.5405	0.0697								
S2.E	Pre (RWS)	1.4409	0.7726	0.116	N/A	616†	12	Wilcoxon	<0.001	***	AUC ((ΔF*t)/F	IN
	Post (RWS)	0.9525	0.4952	0.0832								
	Pre (RWS+CF)	1.4741	0.4905	0.1679		590†	11	Wilcoxon	<0.001	***		
	Post (RWS+CF)	1.5336	0.643	0.1391								
S2.F	Pre (RWS)	1.4276	1.0298	0.1611	N/A	41†	3	Wilcoxon	0.0048	**	AUC ((ΔF*t)/F	SST
	Post (RWS)	1.1308	0.9495	0.1378								
	Pre (RWS+CF)	1.1075	0.6072	0.294		31†	3	Wilcoxon	0.7539	n.s.		
	Post (RWS+CF)	1.0747	0.5804	0.1862								
S2.G	Pre (RWS)	0.6099	0.3682	0.0767	N/A	83†	5	Wilcoxon	0.0359	*	AUC ((ΔF*t)/F	PV
	Post (RWS)	0.5004	0.3811	0.0651								
	Pre (RWS+CF)	0.5372	0.3252	0.0779		113†	5	Wilcoxon	0.5456	n.s.		
	Post (RWS+CF)	0.5028	0.3527	0.0580								

† indicates whether statistics performed across cells or mice

Data S6.

Data and statistical tests corresponding to Supplementary Figure 2.

panel		mean	median	error	n cells	N mice	test	*P* value	result	measurement (units)	cell type
S3.B	PN	0.0078	-0.0019	0.0023	1147	24	N/A	N/A	N/A	xCorr (r)	PN
	IN	0.0332	0.0123	0.0023	1620	35				xCorr (r)	IN
	PV	-1.47E-04	-2.72E-04	0.0045	221	13				xCorr (r)	PV
	SST	0.041	0.0354	0.0099	91	8				xCorr (r)	SST
	VIP	0.0909	0.0836	0.0078	173	11				xCorr (r)	VIP
S3.D (top l)	Rest	29.61	N/A	9.7967	N/A	12†	Chi-squared	0.01071	*	percent total trials (%)	N/A
	Active	69.84		9.9334							
	Stop	0.55		0.2902							
S3.D (bottom l)	Rest	24.35		9.5786							
	Active	75.29		9.6393							
	Stop	0.36		0.2324							
S3.D (top r)	Rest	33.46		12.1959		11†	Chi-squared	<0.001	***		
	Active	66.54		12.1959							
	Stop	0		0							
S3.D (bottom r)	Rest	42.45		13.1339							
	Active	57.32		13.1921							
	Stop	0.24		0.1441							
S3.H	Pre (RWS)	4.0059	2.1655	0.7509	124†	12	Wilcoxon	0.0147	*	AUC ((ΔF*t)/F)	PN
	Post (RWS)	5.7207	2.2396	1.5931							
	Pre (RWS+CF)	2.677	1.7382	0.1927	388†	11	Wilcoxon	0.5104	n.s.		
	Post (RWS+CF)	2.4344	1.7958	0.1195							
S3.I	Pre (RWS)	3.3914	2.3096	0.2246	212†	12	Wilcoxon	0.0033	**	AUC ((ΔF*t)/F)	IN
	Post (RWS)	2.965	2.0138	0.2076							
	Pre (RWS+CF)	3.3041	2.2275	0.2025	296†	11	Wilcoxon	<0.001	***		
	Post (RWS+CF)	3.5204	2.2994	0.1901							

† indicates whether statistics performed across cells or mice

Data S7.
Data and statistical tests corresponding to Supplementary Figure 3.

panel		mean	error	N mice	test	*P* value	result	measurement (units)
S4.C	RWS (Pre) RWS (Post)	1 3.6978	0 0.8273	4	one-sample t-test	0.0471	*	Whisker responsive area
	RWS+CF (Pre) RWS+CF (Post)	1 0.5195	0 0.2171	4		0.1138	n.s.	
	control (Pre) control (Post)	1 1.5067	0 0.1176	4		0.0649	n.s.	

Data S8.

Data and statistical tests corresponding to Supplementary Figure 4.

panel		mean	median	error	n cells	N mice	test	*P* value	result	measurement (units)
S5.B	Pre	2.8467	2.507	0.1745	220†	3	Pre vs DCZ: Wilcoxon	Pre vs DCZ: <0.001	Pre vs DCZ: ***	AUC ((ΔF*t)/F)
	DCZ	1.587	1.2817	0.0809	218†		DCZ vs Post: Wilcoxon	DCZ vs Post: <0.001	DCZ vs Post: ***	
	Post	1.7015	1.4958	0.0726	220†					
S5.C	Control	0	0.0212	0.0631	218†	3	Wilcoxon	<0.001	***	Relative ΔAUC (Δ((ΔF*t)/F))
	Plasticity	-0.14	-0.2199	0.0509	253†	4				
S5.E	Pre	4.2185	3.0214	0.3601	181†	3	Pre vs DCZ: Wilcoxon	Pre vs DCZ: <0.001	Pre vs DCZ: ***	AUC ((ΔF*t)/F)
	DCZ	2.9159	2.2613	0.2104	177†		DCZ vs Post: Wilcoxon	DCZ vs Post: 0.0422	DCZ vs Post: *	
	Post	2.5923	2.1445	0.1419	177†					
S5.F	Control	0	-0.0686	0.0655	173†	3	Wilcoxon	0.6742	n.s.	Relative ΔAUC (Δ((ΔF*t)/F))
	Plasticity	-2.469	-0.0227	2.9139	164†	3				
S5.H	Pre	4.3825	2.7846	0.425	181†	3	Pre vs DCZ: Wilcoxon	Pre vs DCZ: 0.0018	Pre vs DCZ: **	AUC ((ΔF*t)/F)
	DCZ	4.3789	3.374	0.3058	185†		DCZ vs Post: Wilcoxon	DCZ vs Post: <0.001	DCZ vs Post: ***	
	Post	3.8364	2.8455	0.2325	180†					
S5.I	Control	0	-0.2341	0.0623	175†	3	Wilcoxon	0.0928	n.s.	Relative ΔAUC (Δ((ΔF*t)/F))
	Plasticity	0.1359	0.0253	0.0409	181†	3				
S5.K	Pre	3.093	2.0421	0.2373	363†	4	Pre vs DCZ: Wilcoxon	Pre vs DCZ: < 0.001	***	AUC ((ΔF*t)/F)
	DCZ	9.0378	6.7442	0.3663	368†		DCZ vs Post: Wilcoxon	Pre vs DCZ: <0.001	***	
	Post	6.381	4.7294	0.2822	369†					
S5.L	Control	0	-0.0262	0.0189	368	4	Wilcoxon	<0.001	***	Relative ΔAUC (Δ((ΔF*t)/F))
	Plasticity	0.6522	0.0344	0.0633	258	3				
S5.N	Pre	2.4242	1.9103	0.2445	136†	3	Pre vs DCZ: Wilcoxon	Pre vs DCZ: <0.001	Pre vs DCZ: ***	AUC ((ΔF*t)/F)
	DCZ	3.1922	2.6613	0.2031	137†		DCZ vs Post: Wilcoxon	DCZ vs Post:0.0902	DCZ vs Post: n.s.	
	Post	3.0724	2.5155	0.2135	137†					
S5.O	Control	0	0.0021	0.022	145†	3	Wilcoxon	<0.001	***	Relative ΔAUC (Δ((ΔF*t)/F))
	Plasticity	0.1723	0.0982	0.0351	197†	4				

† indicates whether statistics performed across cells or mice

Data S9.
Data and statistical tests corresponding to Supplementary Figure 5.